

1 Revised for **Journal of Geophysical Research**

2 Effects of the Diurnal Cycle in Solar Radiation on the
3 Tropical Indian Ocean Mixed Layer Variability during
4 Wintertime Madden-Julian Oscillations

5 Yuanlong Li,^{1,*} Weiqing Han,¹ Toshiaki Shinoda,² Chunzai Wang,³
6 Ren-Chieh Lien,⁴ James N. Moum,⁵ Jih-Wang Wang⁶

7 1. Department of Atmospheric and Oceanic Sciences, University of Colorado, Boulder, Colorado

8 2. Naval Research Laboratory, Stennis Space Center, Mississippi

9 3. NOAA/Atlantic Oceanographic and Meteorological Laboratory, Miami, Florida

10 4. Applied Physics Laboratory, University of Washington, Seattle, Washington

11 5. College of Earth, Ocean and Atmospheric Sciences, Oregon State University, Corvallis, Oregon

12 6. Cooperative Institute for Research in Environmental Sciences, Boulder, Colorado

13 September 2013

* **Corresponding Author Address:** Department of Atmospheric and Oceanic Sciences, University of Colorado, Campus Box 311, Boulder, CO 80309, USA; Email: yuanlong.li@colorado.edu

14 **Abstract**

15 The effects of solar radiation diurnal cycle on intraseasonal mixed layer variability
16 in the tropical Indian Ocean during boreal wintertime Madden-Julian Oscillation (MJO)
17 events are examined using the HYbrid Coordinate Ocean Model. Two parallel
18 experiments, the main run and the experimental run, are performed for the period of
19 2005-2011 with daily atmospheric forcing except that an idealized hourly shortwave
20 radiation diurnal cycle is included in the main run. The results show that the diurnal
21 cycle of solar radiation generally warms the Indian Ocean sea surface temperature (SST)
22 north of 10°S, particularly during the calm phase of the MJO when sea surface wind is
23 weak, mixed layer is thin, and the SST diurnal cycle amplitude ($dSST$) is large. The
24 diurnal cycle enhances the MJO-forced intraseasonal SST variability by about 20% in
25 key regions like the Seychelles–Chagos Thermocline Ridge (SCTR; 55°-70°E, 12°-4°S)
26 and the central equatorial Indian Ocean (CEIO; 65°-95°E, 3°S-3°N) primarily through
27 nonlinear rectification. The model also well reproduced the upper-ocean variations
28 monitored by the CINDY/DYNAMO field campaign between September-November
29 2011. During this period, $dSST$ reaches 0.7°C in the CEIO region, and intraseasonal SST
30 variability is significantly amplified. In the SCTR region where mean easterly winds are
31 strong during this period, diurnal SST variation and its impact on intraseasonal ocean
32 variability are much weaker. In both regions, the diurnal cycle also has large impact on
33 the upward surface turbulent heat flux Q_T and induces diurnal variation of Q_T with a
34 peak-to-peak difference of $O(10 \text{ W m}^{-2})$.

35 **1. Introduction**

36 **1.1. MJO and Indian Ocean Intraseasonal Variability**

37 As the major mode of intraseasonal variability of the tropical atmosphere, the
38 Madden–Julian Oscillation (MJO) [*Madden and Julian, 1971*] has a profound climatic
39 impact at global scale [e.g., *Zhang, 2005*]. The MJO is characterized by large-scale
40 fluctuations of atmospheric deep convection and low-level winds at periods of 20–90
41 days, and propagates eastward at a mean speed of 5 m s^{-1} over warm areas of the
42 tropical Indian and Pacific Oceans. At the lowest order, the MJO was considered to be
43 an intrinsic convection-wind coupling mode of the tropical atmosphere [e.g., *Knutson*
44 *and Weickmann, 1987; Wang and Rui, 1990; Zhang and Dong, 2004*]. Recently, the role
45 of air-sea interaction in the MJO dynamics is receiving increasing interest. As a major
46 source of heat and moisture, the mixed layer of the tropical Indian Ocean (TIO) plays an
47 important role in the initiation and development of the MJO convection. Modeling
48 studies demonstrate that including air-sea coupling on intraseasonal timescale can
49 improve the simulation [e.g., *Wang and Xie, 1998; Waliser et al., 1999; Woolnough et*
50 *al., 2001; Inness and Slingo, 2003; Inness et al., 2003; Sperber et al., 2005; Zhang et al.,*
51 *2006; Watterson and Syktus, 2007; Yang et al., 2012*] and forecast [e.g., *Waliser, 2005;*
52 *Woolnough et al., 2007*] of the MJO behaviors. However, because the MJO-related
53 air-sea coupling processes are not well understood, realistically representing the MJO is
54 still a challenging task for the state-of-the-art climate models [e.g., *Lin et al., 2006;*
55 *Zhang et al., 2006; Lau et al., 2012; Sato et al., 2012; Xavier et al., 2012*]. Given that
56 the tropical ocean affects the atmosphere through mainly sea surface temperature (SST),
57 investigating the TIO intraseasonal SST variability and associated upper-ocean

58 processes will help improve our understanding of air-sea interaction processes on
59 intraseasonal timescale.

60 With the advent of satellite microwave SST products, strong intraseasonal SST
61 signals with 1-2°C magnitudes have been detected in the TIO [e.g., *Harrison and Vecchi*,
62 2001; *Sengupta et al.*, 2001; *Duvel et al.*, 2004; *Saji et al.*, 2006; *Duvel and Vialard*,
63 2007]. During boreal winter, the strong 20-90-day SST variability in the southern TIO,
64 particularly in the Seychelles–Chagos Thermocline Ridge (SCTR) region [*Hermes and*
65 *Reason*, 2008], is shown to be associated with wintertime MJO events [e.g., *Waliser et*
66 *al.*, 2003; *Duvel et al.*, 2004; *Saji et al.*, 2006; *Duvel and Vialard*, 2007; *Han et al.*, 2007;
67 *Vinayachandran and Saji*, 2008; *Izumo et al.*, 2010; *Lloyd and Vecchi*, 2010; *Jayakumar*
68 *et al.*, 2011; *Jayakumar and Gnanaseelan*, 2012]. During boreal winter, SST in the
69 SCTR is high, but the thermocline and mixed layer depth (MLD) are shallow due to the
70 Ekman upwelling induced by the large-scale wind stress curl [*McCreary et al.*, 1993;
71 *Xie et al.*, 2002; *Schott et al.*, 2009]. These mean conditions favor large-amplitude SST
72 response to intraseasonal radiation and wind changes associated with the MJO. In
73 addition, the SCTR is located at the western edge of the inter-tropical convergence zone
74 (ITCZ) and close to the initiation area of most strong wintertime MJO events [*Wheeler*
75 *and Hendon*, 2004; *Zhang*, 2005; *Zhao et al.*, 2013]. In this region, relatively small
76 changes in SST may induce significant perturbations in atmospheric convection and thus
77 may have profound impacts on weather and climate [*Xie et al.*, 2002; *Vialard et al.*,
78 2009]. The feedbacks of SST anomalies (SSTA) onto the atmosphere are believed to be
79 essential in organizing the large-scale convection and facilitating the eastward
80 propagation of the MJO [e.g., *Flatau et al.*, 1997; *Woolnough et al.*, 2001, 2007;
81 *Bellenger et al.*, 2009; *Webber et al.*, 2012], and also important in determining their

82 phase, time scale, spatial structure, and propagation paths [e.g., *Saji et al.*, 2006; *Izumo*
83 *et al.*, 2010].

84 The mechanism that controls intraseasonal SST variability is, however, still under
85 debate. While some studies emphasize the importance of wind forcing and ocean
86 dynamics [*Harrison and Vecchi*, 2001; *Saji et al.*, 2006; *Han et al.*, 2007;
87 *Vinayachandran and Saji*, 2008], others show the significant effects of shortwave
88 radiation [*Duvel et al.*, 2004; *Duvel and Vialard*, 2007, *Vialard et al.*, 2008; *Zhang et al.*,
89 2010; *Jayakumar et al.*, 2011; *Jayakumar and Gnanaseelan*, 2012]. To improve our
90 understanding of the intraseasonal TIO SST variability and its feedbacks to the MJO
91 convection, further investigation is needed to address other involved processes, such as
92 the diurnal cycle's effects.

93 **1.2. Diurnal Cycle of SST**

94 Due to the large day/night difference in solar radiation, SST exhibits
95 large-amplitude diurnal variation [*Sverdrup et al.*, 1942]. Since the 1960s, large diurnal
96 warming ($dSST$) with magnitude $> 1^{\circ}\text{C}$ has been frequently detected by in-situ and
97 satellite observations throughout the world's oceans [e.g., *Stommel*, 1969; *Halpern and*
98 *Reed*, 1976; *Deschamps and Frouin*, 1984; *Price et al.*, 1986; *Stramma et al.*, 1986]. In
99 the tropics, diurnal warming can reach as large as $2\text{-}3^{\circ}\text{C}$ under clear-sky, low-wind
100 condition [e.g., *Flament et al.*, 1994; *Webster et al.*, 1996; *Soloviev and Lukas*, 1997;
101 *Stuart-Menteth et al.*, 2003; *Kawai and Wada*, 2007; *Kennedy et al.*, 2007; *Gille*, 2012].
102 During the calm (suppressed) phase of the MJO, such condition is satisfied in the TIO.
103 The large daytime ocean warming at the calm phase induces an increase of the net
104 surface heat flux toward the atmosphere by $> 50 \text{ W m}^{-2}$ [*Fairall et al.*, 1996], which can

105 significantly alter the vertical distributions of heat, moisture, and buoyance of the
106 atmosphere, and thereby influence the formation and development of the MJO
107 convection system [*Webster et al.*, 1996; *Woolnough et al.*, 2000, 2001; *Yang and Slingo*,
108 2001; *Slingo et al.*, 2003; *Dai and Trenberth*, 2004; *Bellenger et al.*, 2010].

109 Except for a direct feedback to the atmosphere, the diurnal ocean variation can also
110 impact intraseasonal SST variability associated with the MJO. Recent modeling studies
111 showed that resolving the diurnal cycle of solar radiation forcing in ocean models
112 amplifies the intraseasonal SST variability by about 20%-30% in the tropical oceans
113 [*Shinoda and Hendon*, 1998; *McCreary et al.*, 2001; *Bernie et al.*, 2005, 2007; *Shinoda*,
114 2005; *Guemas et al.*, 2011] via nonlinear effect [*Shinoda and Hendon*, 1998; *Bernie et*
115 *al.*, 2005; *Shinoda*, 2005]. During daytime, strong shortwave heating Q_{SW} stabilizes the
116 upper ocean and thins the mixed layer. As a result, a large amount of Q_{SW} is absorbed by
117 the upper few meters of the ocean, which significantly increases the SST. At night,
118 cooling destabilizes the upper ocean and erodes the diurnal warm layer created during
119 daytime. However, further cooling of SST is usually very small because it requires a lot
120 of energy to entrain deeper water into the mixed layer [*Shinoda*, 2005]. As a result, the
121 daily mean SST is higher with the diurnal cycle forcing of Q_{SW} . This effect primarily
122 occurs during the calm phase of the MJO when high insolation and low winds produce a
123 thin mixed layer and a strong SST diurnal cycle, which can therefore enhance the
124 intraseasonal SST variability associated with the MJO. Such effect may also contribute
125 to the underestimation of the MJO signals in coupled models that do not resolve the
126 diurnal cycle [e.g., *Inness and Slingo*, 2003; *Zhang et al.*, 2006].

127 Modeling studies also suggest that the diurnal cycle of solar radiation can modify
128 the mean state of the tropical oceans [e.g., *Schiller and Godfrey*, 2003; *Bernie et al.*,

129 2007, 2008] and improve the simulation of large-scale tropical climate variability such
130 as the MJO [*Woolnough et al.*, 2007; *Bernie et al.*, 2008; *Oh et al.*, 2012], Indian
131 Monsoon [*Terray et al.*, 2012], and El Niño-Southern Oscillation (ENSO)
132 [*Danabasoglu et al.*, 2006; *Masson et al.*, 2012]. These findings have greatly improved
133 our understanding of the role of the diurnal cycle in the tropical climate system.
134 Amongst the existing studies, however, investigations of diurnal ocean variation are
135 mainly for the western Pacific warm pool region [*Shinoda and Hendon*, 1998; *Bernie et*
136 *al.*, 2005; *Shinoda*, 2005] or the Atlantic Ocean [*Pimental et al.*, 2008; *Guemas et al.*,
137 2011], whereas coupled model studies focus primarily on the general effects of diurnal
138 coupling on the mean structure and low-frequency variability of the climate
139 [*Danabasoglu et al.*, 2006; *Bernie et al.*, 2008; *Noh et al.*, 2011; *Oh et al.*, 2012;
140 *Masson et al.*, 2012; *Guemas et al.*, 2013]. In the present study, we examine the effects
141 of diurnal cycle on the intraseasonal SST variability in the TIO region where many
142 winter MJO events originate, which has not yet been sufficiently explored by previous
143 researches.

144 **1.3. CINDY/DYNAMO Field Campaign**

145 DYNAMO (Dynamics of the MJO; <http://www.eol.ucar.edu/projects/dynamo/>) is a
146 US program that aims to advance our understanding of processes key to MJO initiation
147 over the Indian Ocean and therefore improve the MJO simulation and prediction. As the
148 first step, the DYNAMO joined the international field program of CINDY (Cooperative
149 Indian Ocean Experiment on Intraseasonal Variability) in 2011 to collect in-situ
150 observations [*Zhang et al.*, 2013]. The CINDY/DYNAMO field campaign [*Yoneyama et*
151 *al.*, 2013] took place in the central equatorial Indian Ocean (CEIO) during September

152 2011 - March 2012. These field observations will serve as constraints and validation for
153 modeling studies. Its atmospheric component includes two intensive sounding arrays, a
154 multiple wavelength radar network, a ship/mooring network to measure air-sea fluxes,
155 the marine atmospheric boundary layer, and aircraft operations to measure the
156 atmospheric boundary layer and troposphere property variations. The oceanic
157 component includes an array of surface buoys and conductivity–temperature–depth
158 (CTD) casts from research vessels in the CEIO. During the monitor period, active
159 episodes of large-scale convection associated with wintertime MJOs were observed to
160 propagate eastward across the TIO [*Shinoda et al.*, 2013b]. The synchronous records of
161 oceanic variability during MJO events are used here to validate the model simulations
162 and examine the potentially crucial upper-ocean processes in the MJO initiation.

163 **1.4. Present Research**

164 The present study has two objectives. First, by including the diurnal cycle of solar
165 radiation in the forcing fields of a high-resolution ocean general circulation model
166 (OGCM), we aim to examine the effects of the diurnal cycle on intraseasonal variability
167 of the surface mixed layer in the TIO. Particular attention will be paid to the SCTR and
168 CEIO regions, which are important regions for wintertime MJO initiation and
169 propagation. Second, we specifically investigate how the Q_{SW} diurnal cycle influences
170 intraseasonal oceanic variability and feedbacks to surface heat flux during the
171 CINDY/DYNAMO field campaign. The results are expected to complement our
172 knowledge of air-sea interaction associated with MJO dynamics and hence contribute to
173 the DYNAMO program. The rest of the paper is organized as follows. Section 2
174 outlines the OGCM configurations and experiment design. Section 3 provides a

175 comprehensive comparison of the model results with available in-situ/satellite
176 observations. Section 4 reports our major research findings. Finally, Section 5 provides
177 the summary and discussion.

178 **2. Model and Experiments**

179 **2.1. Model Configuration**

180 The OGCM used in this study is the HYbrid Coordinate Ocean Model (HYCOM)
181 version 2.2.18, in which isopycnal, sigma (terrain-following), and z-level coordinates
182 are combined to optimize the representation of oceanic processes [Bleck, 2002;
183 Halliwell, 2004; Wallcraft *et al.*, 2009]. In recent researches HYCOM has been
184 successfully used to investigate a wide range of ocean processes at various timescales in
185 the Indo-Pacific and tropical Atlantic Oceans [e.g., Han *et al.*, 2006, 2007, 2008; Yuan
186 and Han, 2006; Kelly *et al.*, 2007; Kara *et al.*, 2008; Duncan and Han, 2009; Metzger *et*
187 *al.*, 2010; Nyadjro *et al.*, 2012; Shinoda *et al.*, 2012; Wang *et al.*, 2012a, 2012b]. In this
188 study, HYCOM is configured to the tropical and subtropical Indo-Pacific basin
189 (30°E-70°W, 40°S-40°N) with a horizontal resolution of 0.25°×0.25°. Realistic marine
190 bathymetry from the National Geophysical Data Center (NGDC) 2' digital data are used
191 with 1.5°×1.5° smoothing. The smoothed bathymetry is carefully checked and
192 compared with the General Bathymetric Chart of the Oceans (GEBCO) [Smith and
193 Sandwell, 1997] in the Indonesian Seas to ensure the important passages of the
194 throughflow are well resolved. No-slip conditions are applied along continental
195 boundaries. At the open-ocean boundaries near 40°S and 40°N, 5° sponge layers are
196 applied to relax the model temperature and salinity fields to the World Ocean Atlas 2009
197 (WOA09) annual climatological values [Antonov *et al.*, 2010; Locarnini *et al.*, 2010].

198 The model has 35 vertical layers, with 10 layers in the top 11 m to resolve the
199 diurnal warm layer. *Bernie et al.* [2005] suggested that for the K-Profile
200 Parameterization (KPP), the thickness of the uppermost layer is critical in resolving the
201 diurnal SST variation. In our model, the thickness of the uppermost layer is set to be
202 0.52 m. The thickness gradually increases with depth. In most areas of the open ocean,
203 the mean layer thickness is smaller than 5, 10, and 20 m in the upper 100, 200, and 500
204 m, respectively. The diffusion/mixing parameters of the model are identical to those
205 used in *Wang et al.* [2012a]. The nonlocal KPP [*Large et al.*, 1994, 1997] mixing
206 scheme is used. Background diffusivity for internal wave mixing is set to $5 \times 10^{-6} \text{ m}^2 \text{ s}^{-1}$
207 [*Gregg et al.*, 2003], and viscosity is set to be one order larger ($5 \times 10^{-5} \text{ m}^2 \text{ s}^{-1}$) [*Large et*
208 *al.*, 1994]. The diapycnal mixing coefficient is $(1 \times 10^{-7} \text{ m}^2 \text{ s}^{-2}) N^{-1}$, where N is the
209 Brunt–Väisälä frequency. Isopycnal diffusivity and viscosity values are parameterized
210 as $u_d \Delta x$, where Δx is the local horizontal mesh size, and u_d is the dissipation velocity.
211 We set $u_d = 1.5 \times 10^{-2} \text{ m s}^{-1}$ for Laplacian mixing and $5 \times 10^{-3} \text{ m s}^{-1}$ for biharmonic mixing
212 of momentum, and $u_d = 1 \times 10^{-3} \text{ m s}^{-1}$ for Laplacian mixing of temperature and salinity.
213 Shortwave radiation Q_{SW} penetration is computed using Jerlov water type I [*Jerlov,*
214 1976].

215 **2.2. Forcing Fields**

216 The surface forcing fields of HYCOM include 2-m air temperature and humidity,
217 surface net shortwave and longwave radiation (Q_{SW} and Q_{LW}), precipitation, 10-m wind
218 speed, and wind stress. The turbulent heat flux Q_T , which consists of the latent and
219 sensible heat fluxes, are not treated as external forcing but automatically estimated by
220 the model with wind speed, air temperature, specific humidity, and SST, using the

221 Coupled Ocean-Atmosphere Response Experiment (COARE 3.0) algorithm [*Fairall et*
222 *al.*, 2003; *Kara et al.*, 2005]. In our experiments, the 2-m air temperature and humidity
223 are adopted from the European Centre for Medium-Range Weather Forecasts (ECMWF)
224 Re-analysis Interim (ERA-Interim) products [*Dee et al.*, 2011], which have a 0.7°
225 horizontal resolution available for the period of 1989–2011.

226 For the surface shortwave and longwave radiation, we use the daily, geostationary
227 enhanced 1° product from Clouds and the Earth's Radiant Energy System (CERES)
228 [*Wielicki et al.*, 1996; *Loeb et al.*, 2001] of the National Aeronautics and Space
229 Administration (NASA) for the period of March 2000—November 2011. Given that
230 Q_{SW} is crucial in modeling intraseasonal and diurnal ocean variability, the quality of the
231 CERES product should be validated. Figure 1 compares the CERES Q_{SW} with in-situ
232 measurements by the Research Moored Array for African–Asian–Australian Monsoon
233 Analysis and Prediction (RAMA) mooring arrays [*McPhaden et al.*, 2009] at three sites
234 in the TIO. The CERES data agree well with RAMA measurements with the correlation
235 coefficients exceeding 0.90 at all the three buoy sites. The mean values and standard
236 deviation (STD) from CERES are close to RAMA measurements, but the CERES STD
237 values are smaller by about 15%. Comparisons are also performed for the Pacific Ocean
238 with the Tropical Atmosphere Ocean/Triangle Trans-Ocean Buoy Network
239 (TAO/TRITON) buoys, and we obtained similar degree of consistency.

240 The $0.25^\circ \times 0.25^\circ$ Cross-Calibrated Multi-Platform (CCMP) ocean surface wind
241 vectors available during July 1987—December 2011 [*Atlas et al.*, 2008] are used as
242 wind forcing. Zonal and meridional surface wind stress, τ_x and τ_y , are calculated from
243 the CCMP 10-m wind speed $|V|$ using the standard bulk formula

$$244 \quad \tau_x = \rho_a c_d |V| u, \quad \tau_y = \rho_a c_d |V| v, \quad (1)$$

245 where $\rho_a = 1.175 \text{ kg m}^{-3}$ is the air density, $c_d = 0.0015$ is the drag coefficient, and u and
 246 v are the zonal and meridional 10-m wind components. The precipitation forcing is from
 247 the $0.25^\circ \times 0.25^\circ$ Tropical Rainfall Measuring Mission (TRMM) Multi-Satellite
 248 Precipitation Analysis (TMPA) level 3B42 product [Kummerow *et al.*, 1998] available
 249 for 1998-2011. In addition to precipitation, river discharge is also important for
 250 simulating upper-ocean salinity distribution in the Bay of Bengal (BoB) [e.g., Han and
 251 McCreary, 2001], which influences the stratification and circulation of the TIO. In our
 252 experiments, we utilize the satellite-derived monthly discharge records of the
 253 Ganga-Brahmaputra [Papa *et al.*, 2010] and monthly discharge data from Dai *et al.*
 254 [2009] for the other BoB rivers such as the Irrawaddy as the lateral fresh water flux
 255 forcing.

256 **2.3. Experiments**

257 The model is spun-up for 35 years from a state of rest, using WOA09 annual
 258 climatology of temperature and salinity as the initial condition. Datasets described
 259 above are averaged into monthly climatology and linearly interpolated onto the model
 260 grids to force the spin-up run. Restarting from the already spun-up solution, HYCOM is
 261 integrated forward from January 1 2005 to November 30 2011. Two parallel
 262 experiments are performed, the main run (MR) and the experimental run (EXP), using
 263 daily atmospheric forcing fields. The only difference between the MR and EXP is that in
 264 the MR an idealized hourly diurnal cycle is imposed on Q_{sw} , which is assumed to be
 265 sinusoidal and energy-conserving [Shinoda and Hendon, 1998; Schiller and Godfrey,
 266 2003; Shinoda, 2005],

$$267 \quad Q_{sw}(t) = \begin{cases} \pi Q_{sw0} \sin[2\pi(t-6)/24] & \text{for } 6 \leq t \leq 18 \\ 0 & \text{for } 0 \leq t \leq 6 \text{ or } 18 \leq t \leq 24 \end{cases} \quad (2)$$

268 where t is the local standard time (LST) in hours, and Q_{SW0} is the daily mean value of
269 Q_{SW} . Hence the difference between the MR and EXP isolates the impact of the solar
270 radiation diurnal cycle. Both the two experiments are integrated for around 7 years from
271 January 2005 to November 2011, with the outputs stored in daily resolution. In addition,
272 0.1-day (2.4-hour) output from MR is also stored for the period overlapping the
273 CINDY/DYNAMO field campaign (September-November 2011) to better resolve the
274 ocean diurnal variation. In order to avoid the transitioning effect from the spin-up, only
275 the 2006-2011 output is used for analysis. Noted that the $0.25^\circ \times 0.25^\circ$ resolution allows
276 the model to resolve eddies resulting from oceanic internal variability. This effect is
277 contained in the difference solution MR-EXP and will be discussed in Section 5.

278 **3. Model/Data Comparison**

279 **3.1. Comparisons with In-Situ and Satellite Observations**

280 To validate the model performance, we compare the output of HYCOM MR with
281 available in-situ and satellite observations. During the 2006-2011 period, the wintertime
282 mean SST from HYCOM MR is quite similar to that from the TRMM Microwave
283 Instrument (TMI) data [*Wentz et al.*, 2000] (Figures 2a and 2b). In the TIO, both the
284 SCTR (55° - 70° E, 12° - 4° S) and CEIO (65° - 95° E, 3° S- 3° N) regions are covered by weak
285 winds and characterized by high SST ($> 29^\circ$ C) values during winter, which are well
286 simulated by the model. Major discrepancies occur in the western tropical Pacific,
287 where the simulated warm pool (SST $> 28^\circ$ C region) is larger in size than TMI
288 observations. The modeled sea surface salinity (SSS) pattern also agrees with the in-situ
289 observational dataset of the Grid Point Value of the Monthly Objective Analysis

290 (MOAA-GPV) data [*Hosoda et al.*, 2008] (Figures 2c and 2d), which includes data
291 records from Argo floats, buoy measurements, and casts of research cruises. Note that
292 SSS in the MOAA-GPV is represented by salinity at 10 dbar, which is the shallowest
293 level of the dataset, whereas HYCOM SSS is near the surface (~ 0.26 m). While the
294 model and observation reach a good overall agreement, the MR SSS is somewhat higher
295 in the subtropical South Indian Ocean, Arabian Sea, and western BoB. In the regions of
296 our interest, the SCTR and CEIO, however, the modeled SSS values are close to the
297 observations.

298 The wintertime mean MLD values from the MOAA-GPV and HYCOM MR agree
299 well in the two key regions (Figure 3). They show consistent large-scale spatial patterns
300 over the Indian Ocean. Here, the MLD is defined as the depth at which the potential
301 density difference $\Delta\sigma$ from the surface value is equal to equivalent temperature decrease
302 of 0.5°C [*de Boyer Montégut et al.*, 2004],

$$303 \quad \Delta\sigma = \sigma(T_0-0.5, S_0, P_0) - \sigma(T_0, S_0, P_0), \quad (3)$$

304 where T_0 , S_0 , and P_0 are temperature, salinity, and pressure at the sea surface,
305 respectively. Apparent discrepancies occur in the southeastern TIO, Arabian Sea, and
306 BoB, where the modeled MLD is systematically deeper than the observations by about
307 10-20 m. Possible causes for this difference are uncertainties in the forcing fields that
308 may result in errors in oceanic stratification and mixing and model parameterization of
309 turbulent mixing.

310 The seasonal cycle and interannual variations of modeled SST averaged over the
311 Indian Ocean, also agree with TMI data (Figure 4a). There is a mean warming bias of
312 $\sim 0.26^\circ\text{C}$ during the experiment period (2005-2011), which arises mainly from boreal
313 summer (May-October) SST bias. During winter, however, the model and satellite

314 observation agree well (Figure 4a). The vertical temperature profiles averaged in the
315 SCTR and CEIO regions from the MR show general agreements with the MOAA-GPV
316 dataset (Figures 4b and 4c), with model/data deviations occurring primarily in the
317 thermocline layer. The model has a more diffusive thermocline and thus shows artificial
318 warming between 100-400 m, which is a common bias among most existing OGCMs.

319 Daily time series of modeled SST, which includes variability from synoptic to
320 interannual timescales, at two RAMA buoy locations (67°E, 1.5°S within the SCTR and
321 80.5°E, 1.5°S within the CEIO) are compared with the RAMA and TMI observations in
322 Figures 5. MR/RAMA correlations are 0.72 at the SCTR location and 0.85 at the CEIO
323 location, which are higher than the corresponding MR/TMI correlation values (0.65 and
324 0.61). It is noticeable that the TMI SST (red curves) exhibits intensive high-frequency
325 warming/cooling events which are absent in both the HYCOM MR and RAMA buoy
326 observation. Correspondingly, in the spectral space, although intraseasonal SST
327 variances at 20-90-day period are statistically significant at 95% level in all the three
328 datasets, the power at 20-50-day period is visibly higher in TMI than in the other two
329 (Figures 5b and 5d). The variances of the HYCOM MR and RAMA buoys agree quite
330 well with each other in both temporal and spectral spaces. Differences amongst datasets
331 may arise from the definition of SST. The satellite microwave instruments measure the
332 skin temperature of the ocean, which contains the signals of skin effect that can often
333 reach several degrees of variability amplitudes [*Saunders, 1967; Yokoyama et al., 1995;*
334 *Kawai and Wada, 2007*]. The modeled and buoy-measured SSTs represent temperatures
335 at 0.26 m and 1.5 m respectively, which contain little impact from the skin effect.

336 **3.2. Comparison with CINDY/DYNAMO Field Campaign Data**

337 Oceanic in-situ measurements of the CINDY/DYNAMO field campaign cover the
338 period of September 2011-March 2012. Our HYCOM simulation, however, ends at
339 November 29 2011 due to the availability of forcing fields, particularly CERES
340 radiation and CCMP winds. Consequently, the comparison will focus on their
341 overlapping period of September-November 2011 (referred to as “the campaign period”
342 hereafter). Figure 6 shows the time series during the campaign period at 95°E, 5°S
343 where hourly RAMA buoy temperature record is available. We resample the hourly
344 RAMA 1.5-m temperature records to 0.1-day LST to match our MR output. The
345 amplitudes of simulated SST diurnal cycle and their intraseasonal variability are well
346 represented by the model. Both the model and observations show amplified diurnal
347 cycle amplitudes during 9/25-10/05, 10/10-10/16, 11/03-11/16, and 11/22-11/26, and
348 weakened amplitudes during the remaining periods. It is discernible that large (small)
349 $dSST$ values occur during intraseasonal warming (cooling) periods, which will be
350 further investigated in Section 4. Note that there are several large diurnal warming
351 events with $dSST > 1^{\circ}\text{C}$ in the MR 0.26-m temperature (blue curve), which correspond
352 to much weaker amplitudes in the RAMA 1.5-m temperature (red curve). The MR
353 1.5-m temperature (green curve) confirms that those large $dSST$ signals are due to the
354 formation of the thin diurnal warm layer (compare the blue and green curves) [e.g.,
355 *Kawai and Wada, 2007*]. These large events occur in November when maximum solar
356 insolation and the ITCZ migrate to the southern TIO. Enhanced insolation and relaxed
357 winds give rise to large diurnal warming events based on the results from previous
358 observational studies.

359 The upper-ocean thermal structure and its temporal evolution are reasonably
360 simulated by HYCOM during the DYNAMO field campaign at two buoy locations in

361 the CEIO (Figures 7a-7d). For example, the vertical displacements of the MLD (blue
362 curve) are generally consistent with buoy observations, albeit with detailed
363 discrepancies, which are partly attributable to internal variability of the ocean. The
364 modeled thermocline, however, is more diffusive than the observations, consistent with
365 Figure 4. The intraseasonal variations of SST associated with the MJO events are well
366 reproduced by the model, with a linear correlation exceeding 0.8 at both sites, even
367 though the cooling during 10/26-11/10 at 79°E, 0° (Figure 7e) is significantly
368 underestimated.

369 In this section, we have validated the model with independent observational
370 datasets based on satellite, buoy, and Argo measurements. The comprehensive
371 comparison demonstrates that albeit with some biases, HYCOM is able to properly
372 simulate the TIO upper-ocean mean state and variability at various timescales, and thus
373 can be used to examine the impact of the diurnal cycle of solar radiation on the
374 intraseasonal mixed layer variability associated with MJO events.

375 **4. Effects of Diurnal Cycle on the TIO**

376 **4.1. Effects during the 2006-2011 Period**

377 **4.1.1. Impacts on the Mean Fields**

378 To isolate the impact of the diurnal cycle of solar radiation, we examine the
379 difference solution MR–EXP. Figure 8a shows the wintertime mean daily SST
380 difference, Δ SST, where the symbol “ Δ ” denotes the difference between MR and EXP
381 for daily mean variables. Consistent with previous studies based on 1-D model solutions
382 (section 1.2), the diurnal cycle leads to a general surface warming and thus increases the
383 mean SST in the TIO north of 10°S and the western equatorial Pacific. In the SCTR and

384 CEIO regions, the warming effect exceeds 0.1°C , and the mean MLD is shoaled by
385 around 4-8 m (Figure 8b). In the BoB and central-eastern Indian Ocean south of 10°S ,
386 MLD is deepened. In most areas, deepened (shoaled) MLD corresponds to decreased
387 (increased) SST. This is consistent with the fact that a deepened MLD involves
388 entrainment of colder water and thus leads to SST cooling. An exception is in the
389 central-northern BoB, where the diurnal cycle causes MLD deepening by ~ 10 m but
390 SST increasing. This may be attributable to the strong haline stratification near the
391 surface due to monsoon rainfall and river discharge, which leads to the existence of the
392 barrier layer and temperature inversion [e.g., *Vinayachandran et al.*, 2002; *Thadathil et*
393 *al.*, 2007; *Girishkumar et al.*, 2011]. As a result, relatively warmer water is entrained to
394 the surface mixed layer by the diurnal cycle. To confirm this point, we checked the
395 mean vertical temperature and salinity profiles in the model output. Comparing to those
396 in the Arabian Sea and the subtropical South Indian Ocean, the mean vertical
397 temperature gradient in the upper 100 m is much smaller in the central-northern BoB.
398 The stratification in this region relies greatly on salinity gradient; and vertical
399 temperature inversions often occur (not shown; also see *Wang et al.* [2012b]). Such
400 vertical temperature distribution favors the rectified warming effect by the diurnal cycle.

401 **4.1.2. Impacts on Intraseasonal SST**

402 To achieve our goal of understanding the diurnal cycle effect on intraseasonal SST
403 variability associated with the MJO, we first apply a 20-90-day Lanczos digital
404 band-pass filter [*Duchon*, 1979] to isolate intraseasonal SST variability. The wintertime
405 STD maps of 20-90-day SST from TMI satellite observation and HYCOM MR are
406 shown in Figures 9a and 9b. The model, however, generally underestimates the
407 amplitude of intraseasonal SST variability. In the SCTR and CEIO regions, the

408 underestimation is about 20%. This model/data discrepancy is attributable to at least two
409 factors. First, TMI measures the skin temperature of the ocean, which has larger
410 intraseasonal variability amplitudes than the bulk layer temperature (see Figure 5).
411 Second, the somewhat underestimation of radiation variability in CERES dataset
412 (Figure 1) and uncertainty in other forcing fields may also contribute. In spite of the
413 quantitative differences, the general patterns of STD from HYCOM MR agree with
414 satellite observation.

415 The diurnal cycle acts to enhance 20-90-day SST variability in most regions of the
416 TIO, as shown by the STD difference between the MR and EXP (Figure 9c). In the
417 SCTR and CEIO regions, the strengthening magnitude exceeds 0.05°C at some grid
418 points. To better quantify such impact, we calculate the ratio of STD difference relative
419 to the STD value in EXP (Figure 9d),

$$420 \quad R a t i o = \frac{S T D_{M R} - S T D_{E X P}}{S T D_{E X P}} \times 100 \%, \quad (4)$$

421 where STD_{MR} and STD_{EXP} are the 20-90-day SST STDs from MR and EXP, respectively.
422 The ratio generally exceeds 15% and occasionally reaches 20%-30% in some areas of
423 the CEIO. In the SCTR, the overall ratio is positive but pattern is incoherent, with
424 positive values separated by negative ones. Similar incoherent patterns are seen in other
425 regions, such as near the Somalia coast and in the central-eastern South Indian Ocean.
426 Such incoherence is likely induced by oceanic internal variability [e.g., *Jochum and*
427 *Murtugudde, 2005; Zhou et al., 2008*], which show differences between MR and EXP
428 due to their nonlinear nature. As a result, the effect of internal variability is contained in
429 the MR-EXP solution.

430 To reduce the internal variability effect and focus on the pure oceanic response to

431 the MJO forcing, we examine the area-averaged properties over the SCTR and CEIO
432 regions. To identify the strong intraseasonal convection events associated with the MJO
433 and the corresponding SST variability, we obtain the time series of 20-90-day
434 satellite-derived outgoing longwave radiation (OLR) from the National Oceanic and
435 Atmospheric Administration (NOAA) [*Liebmann and Smith, 1996*] averaged over the
436 SCTR and CEIO regions, along with the area-averaged 20-90-day SST from MR and
437 EXP (Figure 10). The 20-90-day OLR and SST have a close association, with all large
438 SST variability events corresponding to strong OLR fluctuations. The lead-lag
439 correlation between OLR and SST during winters of 2006-2011 is significant, with peak
440 values of $r > 0.60$ in both regions when OLR leads SST by 3-4 days. These results
441 suggest that the large-amplitude wintertime intraseasonal SST variability results mainly
442 from the MJO forcing. Both the 20-90-day OLR and SST show clear seasonality in the
443 SCTR, with most strong events happening in winter [*Waliser et al., 2003; Han et al.,*
444 *2007; Vialard et al., 2008*]. Similar seasonality is discernible in the CEIO, although less
445 prominent. The wintertime correlation of 20-90-day OLR time series between the two
446 regions is $r = 0.48$ (significant at 95% confidence level) when the SCTR OLR leads the
447 CEIO one by 2-3 days. This indicates that some of the wintertime MJO events initiated
448 in the SCTR region have a large downstream signature in the CEIO. The diurnal cycle
449 effect on SST is significant in both regions (Figure 10), increasing the STD values by
450 0.03°C and 0.04°C respectively, which means an enhancement of intraseasonal SST
451 variability by $> 20\%$ relative to EXP values. This magnitude is close to the estimations
452 of 20%-30% in the western Pacific warm pool [*Shinoda and Hendon, 1998; Bernie et*
453 *al., 2005, 2007*] and tropical Atlantic Ocean [*Guemas et al., 2011*].

454 Diurnal ocean variation is believed to be potentially important for the air-sea

455 interaction of the MJO, primarily because its rectification on daily mean SST helps to
456 trigger atmospheric convection. To estimate the diurnal cycle impact during different
457 phases of the MJO, we perform a composite analysis based on the 20-90-day OLR
458 values. There are 15 wintertime convection events with 20-90-day OLR reaching
459 minimum (negative) and exceeding 1.5 STD during 2006-2011 in SCTR and 12 events
460 in CEIO region (Figures 10a and 10b), which are used to construct the composite fields.
461 The days with OLR minima are taken as the 0-day phase. Then a 41-day composite
462 MJO event is constructed by simply averaging variables for each day between -20 day
463 and +20 day. Variations of the SCTR region during the composite MJO are shown in
464 Figure 11. The 20-90-day OLR shows two maxima at around the -14 and 14 day,
465 remarking the calm stages of the composite MJO. The total zonal wind (unfiltered) is
466 very weak in the SCTR region (also see Figure 2a) and changes sign with the MJO
467 phases, showing easterlies at the calm stage ($\tau_x = -0.02 \text{ N m}^{-2}$) and westerlies at the wet
468 stage (the 0 day) ($\tau_x = 0.02 \text{ N m}^{-2}$). There is no large difference in wind speed between
469 the calm and wet phases, and therefore the $dSST$ magnitude is primarily controlled by
470 insolation. The diurnal cycle induces $> 0.1^\circ\text{C}$ SST increase and $\sim 5 \text{ m}$ MLD decrease
471 during the calm stage. During the wet phase, $dSST$ is smaller due to the reduced
472 insolation by MJO-associated convective cloud, which results in little rectification on
473 daily mean SST (Figure 11b). The slight deepening of MLD induced by the diurnal
474 cycle (Figure 11c) leads to an entrainment cooling, which also acts to compensate the
475 rectified SST warming by the diurnal cycle.

476 The situation is generally similar in the CEIO except for more prominent changes
477 in wind speed (Figure 11e). The pre-conditioning calm stage is dominated by weak
478 westerlies with $\tau_x = 0.01 \text{ N m}^{-2}$ at -15 day. At the wet phase the westerly wind stress

479 reaches $0.06-0.08 \text{ N m}^{-2}$. Together with changes in insolation, the calm/wet difference in
480 $dSST$ is larger in the CEIO. Consequently, the rectification of the diurnal cycle onto
481 intraseasonal SST variation is larger. During the calm phase, ΔSST reaches as large as
482 0.2°C , whereas at the wet phase ΔSST is very small (Figure 11f). Also different from the
483 SCTR region, the calm stage after the passage of convection center, e.g., during the
484 12-20 day, is characterized by westerly winds with $\tau_x = 0.03-0.04 \text{ N m}^{-2}$. The relatively
485 strong winds suppress diurnal ocean variation and its rectification onto the daily mean
486 SST and MLD. In both regions, the changes of ΔSST can be well explained by MR-EXP
487 difference in the mean mixed layer heating, e.g., the total heat flux Q divided by MLD
488 H (Figures 11d and 11h). This result suggests that in the TIO the diurnal cycle effect on
489 intraseasonal SST variability is primarily through one-dimensional nonlinear
490 rectification via thinning the mixed layer at the calm phase. The entrainment induced by
491 the diurnal cycle seems also contribute to intraseasonal SST variability by cooling daily
492 mean SST at the wet stage, but its role is secondary.

493 **4.2. Effects during CINDY/DYNAMO Field Campaign**

494 The mean patterns of $dSST$, which is defined as the difference between the MR
495 SST maximum between 10:30-21:00 LST and the preceding minimum between
496 0:00-10:30 LST in each day, along with shortwave radiation Q_{SW} and zonal wind stress
497 τ_x , during the campaign period (9/16-11/29 2011) are shown in Figure 12. The diurnal
498 warming is large ($dSST = 0.6-0.9^\circ\text{C}$) along the equator and small ($dSST = 0.1-0.3^\circ\text{C}$)
499 over large areas of the South Indian Ocean (Figure 12a). There is a visible resemblance
500 between $dSST$ pattern with mean Q_{SW} (Figure 12b, which also indicates the diurnal cycle
501 amplitude of Q_{SW}) and wind speed (Figure 12c). For example, large $dSST$ values ($>$

502 0.9°C) in the western equatorial basin, the Mozambique Channel, the Sumatra coast,
503 and marginal seas between Indonesia and Australia all correspond to high Q_{SW} and low
504 wind speed. Both the CEIO and SCTR regions are covered with small Q_{SW} values ($<$
505 240 W m^{-2}), but the CEIO is dominated by weak westerly winds, while the SCTR is
506 with strong easterly winds, which leads to a much larger $dSST$ in the CEIO compared to
507 the SCTR region.

508 During the campaign period, eastward propagation of the 20-90-day OLR signals is
509 quite clear near the equator (Figure 13e) but is less organized within the SCTR latitudes
510 (Figure 13a). Therefore, we define the stages of the MJO events with respect to OLR
511 value in the CEIO region. Two MJO events occurred during the campaign period: MJO
512 1 and MJO 2. The calm stage of MJO 1 (CM-1) is characterized by positive OLR during
513 10/01-10/11 (Figure 13e). It develops during 10/11-10/21 (DV-1), reaches the wet phase
514 (WT-1) during 10/21-10/29, and decays during 10/29-11/8 (DC-1). Our model
515 simulation covers only half of MJO 2: 11/08-11/15 is its calm stage (CM-2); and
516 11/15-11/29 is its developing stage (DV-2). Note that during DV-2, a well-organized
517 strong convection center with 20-90-day OLR $< -30 \text{ W m}^{-2}$ has formed in the SCTR
518 region (Figure 13a), which propagates eastward and reaches the CEIO near the end of
519 our simulation period. While the wind changes associated with MJO 1 are rather
520 disordered, convection center of MJO 2 is accompanied by organized westerly anomaly
521 (relative to the mean easterly wind) over the SCTR (Figure 13b). Daily maps of
522 20-90-day OLR (figures not shown) reveal that convection of MJO 1 is centered north
523 of the equator and shifts northward while propagating eastward, suggesting that MJO 1
524 in October features a typical summertime MJO [e.g., *Waliser et al.*, 2004; *Duncan and*
525 *Han*, 2009; *Vialard et al.*, 2011]. In contrast, MJO 2 is initiated in the SCTR region in

526 November and developed mainly south of the equator, showing typical features of
527 wintertime MJOs.

528 In the map of SSTA for the SCTR, the most evident signal is the seasonal warming
529 from boreal summer to winter (Figure 13c). The only well-organized intraseasonal
530 signature in the SCTR region is the warming during 11/11-11/21 following CM-2 and
531 the subsequent cooling induced by MJO 2. Despite an overall basin-wide warming
532 rectification by the diurnal cycle, Δ SST is in fact negative for the SCTR area during
533 most days in September and October (Figure 13d). There are striking westward
534 propagating signals in Δ SST, which exert visible influence on SSTA (Figure 13c). These
535 signals are likely manifestation of ocean internal variability. In the CEIO, the mean
536 winds are weak westerlies during the campaign period (also see Figure 12c). Hence the
537 eastward propagating westerly wind anomalies following the convection centers (Figure
538 13f) increase the wind speed. The SSTA pattern is clearly dominated by eastward
539 propagating intraseasonal signals associated with the MJOs (Figure 13g), with a visible
540 phase lag of several days to the 20-90-day OLR. Comparing with that in the SCTR
541 region, Δ SST in the CEIO has more systematical contribution to intraseasonal SSTA and
542 amplifies its variability amplitude. For example, large positive Δ SSTs are seen during
543 CM-1, DV-1, CM-2, and DV-2, while near-zero values occurring at WT-1 and DC-1.

544 To reduce the influence of ocean internal variability, we average all the relevant
545 properties over the two regions (Figure 14). In agreement with the preceding analysis,
546 the SCTR region exhibits apparent seasonal transitioning. The easterly winds relax with
547 time (Figure 14a), and SST increases by about 1.3°C during the campaign period
548 (Figure 14b). From September to October, the diurnal cycle has a slight cooling impact
549 on daily mean SST. The only period with a positive Δ SST is 11/08-11/16 that follows

550 the calm stage of MJO 2. After that ΔSST is weak and negative again when the
551 convection center forms. The diurnal cycle amplifies the intraseasonal SST variability
552 for MJO 2 in the SCTR, but the process is somewhat different from the composite MJO,
553 which has near-zero ΔSST at the wet phase. Figures 14c and 14d suggest that while Q/H
554 is not associated with the cooling, the deepened MLD may be responsible. Under strong
555 easterly winds during this period, $dSST$ is small, and MLD is deeper than that in the
556 composite winter MJO event (Figure 11c). Entrainment induced by the diurnal cycle
557 brought deeper, colder water into the mixed layer, which acts to over-compensate the
558 weak rectified warming by $dSST$.

559 In the CEIO, the mean winds are weak, with westerly anomalies following the
560 OLR minima (Figure 14g). The CEIO satisfies low-wind, high-insolation condition at
561 the calm stages and high-wind, low-insolation condition at the wet stages. *Shinoda et al.*
562 [2013a] indicated that extremely weak winds in the CEIO region are mostly responsible
563 for the large diurnal SST variations. Indeed, $dSST$ magnitude at the calm stages is one
564 order larger than at the wet stages (Figure 14h), which enlarges intraseasonal SST
565 amplitude by about 20%-30% through nonlinear effect. Even though the diurnal cycle
566 also deepens MLD in the CEIO at the wet stages, the entrainment does not lead to a SST
567 cooling. Checking the vertical temperature structure indicates that the main thermocline
568 is deeper in the CEIO than in the SCTR (figures not shown). Nighttime deepening of
569 MLD does not reach the cold thermocline water, and thus cannot compensate the
570 rectified warming on daily mean SST by the diurnal cycle.

571 We further assess the diurnal cycle effects on the surface turbulent heat flux toward
572 the atmosphere Q_T which consists of the latent and sensible heat fluxes, $Q_T = Q_L + Q_S$.
573 The latent and sensible heat fluxes can be roughly estimated with the modeled SST and

574 daily wind speed $|V|$ using a standard bulk formula,

$$575 \quad Q_L = \rho_a L_E |V| C_L (q_s - q_a), \quad Q_S = \rho_a C_p |V| C_S (SST - T_a), \quad (5)$$

576 where $\rho_a = 1.175 \text{ kg m}^{-3}$ is the air density, C_L and C_S are respectively latent and sensible
 577 heat transfer coefficients and both assigned a value of 1.3×10^{-3} , $L_E = 2.44 \times 10^6 \text{ J kg}^{-1}$ is
 578 the latent heat of evaporation, $C_p = 1.03 \times 10^3 \text{ J kg}^{-1} \text{ K}^{-1}$ is the specific heat capacity of air,
 579 q_s is the saturation specific humidity at the sea surface, $q_s = q^*(SST)$, where the asterisk
 580 symbol denotes saturation, and q_a is the specific humidity of the air and a function of
 581 the air temperature T_a , $q_a = RH [q^*(T_a)]$. The relative humidity RH is set to be a value of
 582 80% [Waliser and Graham, 1993]. Because T_a closely follows the evolution of SST, we
 583 cannot use the daily 2-m T_a of the ERA-Interim to calculate Q_L and Q_S . Instead, an
 584 empirical estimation method [Waliser and Graham, 1993] is used,

$$585 \quad T_a = \begin{cases} SST - 1.5^\circ C & \text{for } SST < 29^\circ C \\ 27.5^\circ C & \text{for } SST \geq 29^\circ C \end{cases}. \quad (6)$$

586 The 2.4-hour modeled SST from MR are used to calculate the 2.4-hour Q_T and then
 587 averaged into daily Q_T to get comparison with the daily Q_T from EXP (Figures 14e and
 588 14k). Because wind speed is the same for MR and EXP, the MR-EXP difference in
 589 daily Q_T (ΔQ_T) is solely induced by SST difference. In the SCTR, the 11/11-11/21
 590 warming by the diurnal cycle induces an extra heat of $1-2 \text{ W m}^{-2}$, which occurs at the
 591 pre-condition stage of MJO 2. In the CEIO, on the other hand, the diurnal cycle
 592 provides a persistent heating of $1-3 \text{ W m}^{-2}$ for the atmosphere.

593 Comparing with the relatively small correction on daily mean Q_T , the strong Q_T
 594 diurnal cycle, which is obtained by subtracting the daily mean value, is more striking
 595 (Figures 14f and 14l). Due to the large $dSST$, the region-averaged Q_T diurnal difference
 596 can reach $O(10 \text{ W m}^{-2})$ at the pre-condition stages of the MJO. We have also checked

597 the value at specific grid point. At some grids, the Q_T diurnal difference can
598 occasionally reaches as large as 50 W m^{-2} , which is close to the estimation of *Fairall et*
599 *al.* [1996]. Given that the total surface heat flux change associated with the MJO is less
600 than 100 W m^{-2} [e.g., *Shinoda and Hendon*, 1998; *Shinoda et al.*, 1998], diurnal Q_T
601 changes with $O(10 \text{ m}^{-2})$ amplitudes are not negligible for the MJO dynamics. Diurnal
602 heating perturbations with such power can destabilize the low-level atmosphere and
603 contribute to the formation of the MJO convection cluster. For a deeper understanding
604 of how the diurnal variation influences the MJO initiation, air-sea coupling processes at
605 diurnal timescale should be taken into consideration.

606 **5. Discussion and Conclusions**

607 Air-sea interactions in the TIO are believed to be essential in the initiation of MJOs
608 [e.g., *Wang and Xie*, 1998; *Waliser et al.*, 1999; *Woolnough et al.*, 2001; *Zhang et al.*,
609 2006; *Lloyd and Vecchi*, 2010], but the upper-ocean processes associated with
610 intraseasonal SST variability in response to MJOs are not sufficiently understood. One
611 of them is diurnal ocean variation, which is observed to be prominent in the TIO by
612 satellite SST measurements, and suggested to be potentially important in amplifying
613 intraseasonal SST fluctuations and triggering atmospheric convection perturbations at
614 the pre-conditioning stage of MJOs [e.g., *Webster et al.*, 1996; *Shinoda and Hendon*,
615 1998; *Woolnough et al.*, 2000, 2001; *Bernie et al.*, 2005, 2007, 2008; *Bellenger et al.*,
616 2010]. In this study, this process is examined with two HYCOM experiments forced
617 with mainly daily satellite-based atmospheric datasets for the period 2005-2011. The
618 diurnal cycle is included by imposing an hourly idealized Q_{SW} diurnal cycle in MR, and
619 the diurnal cycle effect is quantified by the difference solution, MR-EXP. The

620 experiments also partly cover the time span of CINDY/DYNAMO field campaign. The
621 role of the diurnal cycle in two of the monitored MJO events is particularly evaluated to
622 offer possible contribution for the scientific aim of the DYNAMO program. The model
623 reliability is first validated with available in-situ/satellite observations including buoy
624 measurements of the CINDY/DYNAMO field campaign. The HYCOM MR output
625 agrees reasonably well with observations in both mean-state structure and variability at
626 various timescales. Especially, intraseasonal upper-ocean variations associated with
627 MJOs and the SST diurnal cycle in the TIO are reproduced well.

628 **5.1. Discussion**

629 The sensitivity of the model representation of the SST diurnal cycle to solar
630 radiation absorption profile was discussed by *Shinoda* [2005]. He showed that $dSST$
631 magnitude is sensitive to the choice of different water types, which in turn influence the
632 amplitude of intraseasonal SSTA. In this study we adopt water type I which represents
633 the clearest water with largest penetrating depth for shortwave radiation [*Jerlov*, 1976]
634 for both experiments. Other water types, such as IA and IB (representing less clear
635 water with smaller penetrating depth), are also used to in other testing experiments to
636 evaluate the sensitivity of our results. Indeed, altering the water type to IA or IB leads to
637 some changes in the diurnal cycle's effect. For example, consistent with the result of
638 *Shinoda* [2005], $dSST$ magnitude and its rectification on intraseasonal SSTA are both
639 significantly reduced. Moreover, the mean wintertime ΔSST is changed in magnitude
640 and spatial pattern, with more areas showing negative values. The simulation using
641 water type I achieves the largest degree of consistency with the observation and results
642 of previous studies and is thus adopted in our research. Such sensitivity, however,
643 indicates that to improve the model simulation of the SST diurnal cycle, realistic

644 spatially-varying solar radiation absorption based on Chlorophyll data should be applied
645 instead of using a constant Jerlov water type over the entire model domain.

646 Our interpretation of the diurnal cycle effect suffers from the noising influence of
647 ocean internal variability throughout the analysis, which urges us to provide a particular
648 evaluation of such impact in this section. Figure 15 is the map of root-mean-squared
649 (rms) SST difference between MR and EXP, which quantifies the MR/EXP SST
650 difference at each grid point. The pattern is distinctly different from Figures 8a and 9c.
651 The high value distribution in Figure 15a reminds us the patches of negative values in
652 Figure 9c. The distribution of high-frequency sea surface height (SSH) variability
653 (Figure 15b) confirms that these regions are characterized by intensive ocean internal
654 variability. It means that at a specific grid point the MR/EXP SST difference may reflect
655 mainly the divergence of internal variability signals between MR and EXP rather than
656 the effect of the diurnal cycle. We therefore choose a small region with pronounced
657 internal variability and weak MJO responses to check: 80°-90°E, 20°-10°S. At the
658 center grid (85°E, 15°S) of this box, MR and EXP show large but weakly correlated
659 20-90-day SSTs ($r = 0.19$) (Figure 15c), which suggests that they are mainly induced by
660 ocean internal variability rather than atmospheric forcing. However, averaged over the
661 box, they are greatly reduced in amplitude but highly correlated with each other ($r =$
662 0.92) (Figure 15d). These signals are mainly the ocean's responses to atmospheric
663 intraseasonal oscillations like the MJO, and the rectification by the diurnal cycle is
664 clearly manifested. In Figure 13d we have shown that the diurnal cycle effect on SST in
665 the SCTR is greatly noised by westward propagating signals. Here we further plot out
666 SSH anomalies (SSHA) from MR and EXP at the latitudes of the SCTR (Figure 16).
667 They show generally agreed spatial-temporal patterns, but in fact their difference

668 Δ SSHA is of considerable magnitudes (Figure 16c). The westward propagation speed of
669 Δ SSHA is consistent with that in Figure 13d, confirming the large impact of ocean
670 internal variability on intraseasonal SSTA. However, we have also demonstrated that
671 regional average can effectively reduce such impact and highlight pure ocean responses
672 to atmospheric forcing, especially in a large region like the SCTR where SST responses
673 to MJO events are strong. Therefore, our results derived from analysis of properties
674 averaged for the SCTR and CEIO are generally not largely influenced by ocean internal
675 variability.

676 Another interesting issue is that during the campaign period, the diurnal cycle
677 effect on intraseasonal SSTA is somewhat different from that in the composite MJO. We
678 attribute this to the background conditions like mean-state winds and MLD. This also
679 indicates the sensitivity of ocean diurnal variation and its rectification to the
680 ocean/atmosphere background conditions. Our present modeling work covers only 3
681 months of the CINDY/DYNAMO field campaign and only half of a wintertime MJO
682 event (MJO 2). Analysis of satellite observations suggested that there are three strong
683 winter MJO events occurred during November 2011- March 2012 [*Shinoda et al.*,
684 2013b; *Yoneyama et al.*, 2013]. With the temporal evolution of background conditions in
685 the TIO, the role of the diurnal cycle in each of these events may be different. Extended
686 model experiments covering the whole campaign period are required to examine this
687 event-by-event variance to accomplish our interpretation. Also worth discussing is the
688 method by which we include diurnal variation into the model. We consider an idealized
689 Q_{SW} diurnal cycle and ignore the diurnal variation of wind and precipitation. A better
690 model presentation of the SST diurnal cycle can be achieved in the future research by
691 considering these factors and compared with empirical parametric model predictions to

692 improve our understanding of the controlling processes [e.g., *Webster et al.*, 1996;
693 *Kawai and Kawamura*, 2002; *Clayson and Weitlich*, 2005]. Realistic simulating and
694 in-depth understanding of the ocean diurnal variation and its feedbacks to the
695 atmosphere will eventually contribute to the improvement of climate model prediction.

696 **5.2. Conclusions**

697 Comparison between MR and EXP outputs reveals that over most areas of the TIO,
698 the diurnal cycle of shortwave radiation leads to a mean SST warming by about 0.1°C
699 and MLD shoaling by 2-5 m in winter. The diurnal cycle also acts to enhance the
700 20-90-day SST variability by around 20% in key regions like the SCTR (55°-70°E,
701 12°-4°S) and the CEIO (65°-95°E, 3°S-3°N). Composite analysis for the wintertime
702 MJO events reveals that at the calm stage of the MJO, under high solar insolation and
703 weak sea surface winds, the diurnal SST variation is strong and induces a 0.1-0.2°C
704 increase in Δ SST. At the wet phase, in contrast, Δ SST is near zero because the diurnal
705 ocean variation is suppressed by strong winds and low insolation. This calm/wet
706 contrast hence amplifies the SST response to the MJO, which is consistent with the
707 mechanism proposed by previous studies for the western Pacific warm pool [*Shinoda*
708 *and Hendon*, 1998; *Shinoda*, 2005].

709 The model has also reproduced well the ocean variations associated with two MJO
710 events, MJO 1 and MJO 2, which were monitored by the observation network of the
711 CINDY/DYNAMO field campaign in September-November 2011. During that period,
712 d SST magnitude is around 0.7°C in the CEIO due to weak winds and much smaller in
713 the SCTR. MJO 1 exhibits behaviors typical of summertime MJOs, having limited
714 signature in the SCTR. MJO 2, which occurs in November, is initiated in the vicinity of
715 the SCTR and exhibits winter MJO features. During the two events, the diurnal cycle

716 enhances intraseasonal SST changes in both CEIO and SCTR. Different from the
717 wintertime mean situation, in the campaign period the diurnal cycle causes an overall
718 cooling in the SCTR. This is primarily due to the strong easterly trades and deep
719 mean-state MLD. While large wind speed suppresses ocean diurnal variation and its
720 warming rectification on daily mean SST, deep MLD allows nighttime entrainment to
721 bring cold thermocline water into the mixed layer and thereby over-compensates the
722 rectified heating. Besides the effects on intraseasonal SSTA, diurnal ocean variation also
723 modifies the daily mean Q_T by several W m^{-2} and induces a strong diurnal cycle of it
724 with amplitudes of $O(10 \text{ W m}^{-2})$. Such impact on surface heating have a potential to
725 influence the stability of the low-level atmosphere and trigger convection perturbations
726 associated with MJOs.

727 **Acknowledgements**

728 Y. Li and W. Han are supported by NOAA NA11OAR4310100 and NSF
729 CAREER Award 0847605. Insightful comments by three anonymous reviewers are very
730 helpful in improving our manuscript. We are grateful for the National Center for
731 Atmospheric Research (NCAR) CISL for computational support. The buoy
732 measurements for September-November 2011 used in this study are obtained during
733 CINDY/DYNAMO field campaign (<http://www.jamstec.go.jp/iorgc/cindy/>;
734 <http://www.eol.ucar.edu/projects/dynamo/>). We would like to thank Allan Wallcraft for
735 the technical consultation on HYCOM model and Takeshi Izumo for the benefiting
736 discussion.

737 **Reference**

- 738 Antonov, J. I., D. Seidov, T. P. Boyer, R. A. Locarnini, A. V. Mishonov, H. E. Garcia,
739 O. K. Baranova, M. M. Zweng, and D. R. Johnson (2010), *World Ocean Atlas*
740 *2009, Volume 2: Salinity*, S. Levitus, Ed. NOAA Atlas NESDIS 69, U.S.
741 Government Printing Office, Washington, D.C., 184 pp.
- 742 Atlas, R., J. Ardizzone, and R. N. Hoffman (2008), Application of satellite surface wind
743 data to ocean wind analysis, *Proc. SPIE*, 7087, 70870B, doi:10.1117/12.795371.
- 744 Bellenger, H., J. P. Duvel, M. Lengaigne, and P. Levan (2009), Impact of organized
745 intraseasonal convective perturbations on the tropical circulation, *Geophys. Res.*
746 *Let.*, 36, L16703, doi:10.1029/2009GL039584.
- 747 Bellenger, H., Y. Takayabu, T. Ushiyama, and K. Yoneyama (2010), Role of diurnal
748 warm layers in the diurnal cycle of convection over the tropical Indian Ocean
749 during MISMO, *Month. Wea. Rev.*, 138, 2426-2433.
- 750 Bleck, R. (2002), An oceanic general circulation model framed in hybrid
751 isopycnic-Cartesian coordinates, *Ocean Modell.*, 4, 55-88.
- 752 Bernie, D., E. Guilyardi, G. Madec, J. Slingo, and S. Woolnough (2007), Impact of
753 resolving the diurnal cycle in an ocean-atmosphere GCM. Part 1: a diurnally
754 forced OGCM, *Clim. Dyn.*, 29, 575-590.
- 755 Bernie, D., E. Guilyardi, G. Madec, J. Slingo, S. Woolnough, and J. Cole (2008),
756 Impact of resolving the diurnal cycle in an ocean-atmosphere GCM. Part 2: A
757 diurnally coupled CGCM, *Clim. Dyn.*, 31, 909-925.
- 758 Bernie, D., S. Woolnough, J. Slingo, and E. Guilyardi (2005), Modeling diurnal and
759 intraseasonal variability of the ocean mixed layer, *J. Climate*, 18, 1190-1202.
- 760 Clayson, C. A., and D. Weitlich (2005), Diurnal warming in the tropical Pacific and its
761 interannual variability, *Geophys. Res. Lett.*, 32, L21604,
762 doi:10.1029/2005GL023786.
- 763 Dai, A., T. Qian, K. E. Trenberth, and J. D. Milliman (2009), Changes in continental

764 freshwater discharge from 1948 to 2004, *J. Climate*, 22, 2773-2792.

765 Dai, A., and K. E. Trenberth (2004), The diurnal cycle and its depiction in the
766 Community Climate System Model, *J. Climate*, 17, 930-951.

767 Danabasoglu, G., W. G. Large, J. J. Tribbia, P. R. Gent, B. P. Briegleb, and J. C.
768 McWilliams (2006), Diurnal coupling in the tropical oceans of CCSM3, *J. Climate*,
769 19, 2347-2365.

770 de Boyer Montégut, C., G. Madec, A. S. Fischer, A. Lazar, and D. Iudicone (2004),
771 Mixed layer depth over the global ocean: An examination of profile data and a
772 profile-based climatology, *J. Geophys. Res.*, 109(C12), C12003,
773 doi:10.1029/2004JC002378.

774 Dee, D., S. Uppala, A. Simmons, P. Berrisford, P. Poli, S. Kobayashi, U. Andrae, M.
775 Balsameda, G. Balsamo, and P. Bauer (2011), The ERA-Interim reanalysis:
776 Configuration and performance of the data assimilation system, *Q. J. R. Meteorol.*
777 *Soc.*, 137, 553-597.

778 Deschamps, P., and R. Frouin (1984), Large diurnal heating of the sea surface observed
779 by the HCMR experiment, *J. Phys. Oceanogr.*, 14, 177-184.

780 Duchon, C. E. (1979), Lanczos filtering in one and two dimensions, *J. Appl. Meteor.*, 18,
781 1016–1022.

782 Duncan, B., and W. Han (2009), Indian Ocean intraseasonal sea surface temperature
783 variability during boreal summer: Madden-Julian Oscillation versus submonthly
784 forcing and processes, *J. Geophys. Res.*, 114, C05002, doi:10.1029/2008JC004958.

785 Duvel, J. P., R. Roca, and J. Vialard (2004), Ocean mixed layer temperature variations
786 induced by intraseasonal convective perturbations over the Indian Ocean, *J. Atmos.*
787 *Sci.*, 61, 1004– 1023.

788 Duvel, J. P., and J. Vialard (2007), Indo-Pacific sea surface temperature perturbations
789 associated with intraseasonal oscillations of tropical convection, *J. Climate*, 20,
790 3056-3082.

791 Fairall, C., E. Bradley, J. Godfrey, G. Wick, J. Edson, and G. Young (1996), Cool-skin
792 and warm-layer effects on sea surface temperature, *J. Geophys. Res.*, 101(C1),

793 1295-1308.

794 Fairall, C., E. F. Bradley, J. Hare, A. Grachev, and J. Edson (2003), Bulk
795 parameterization of air-sea fluxes: Updates and verification for the COARE
796 algorithm, *J. Climate*, *16*, 571-591.

797 Flament, P., J. Firing, M. Sawyer, and C. Trefois (1994), Amplitude and horizontal
798 structure of a large diurnal sea surface warming event during the Coastal Ocean
799 Dynamics Experiment, *J. Phys. Oceanogr.*, *24*, 124-139.

800 Flatau, M., P. J. Flatau, P. Phoebus, and P. P. Niiler (1997), The feedback between
801 equatorial convection and local radiative and evaporative processes: The
802 implications for intraseasonal oscillations, *J. Atmos. Sci.*, *54*, 2374–2385.

803 Gille, S. T. (2012), Diurnal variability of upper ocean temperatures from microwave
804 satellite measurements and Argo profiles, *J. Geophys. Res.*, *117*, C11027,
805 doi:10.1029/2012JC007883.

806 Girishkumar, M. S., M. Ravichandran, M. J. McPhaden, and R. R. Rao (2011),
807 Intraseasonal variability in barrier layer thickness in the south central Bay of
808 Bengal, *J. Geophys. Res.*, *116*, C03009, doi :10.1029/2010JC006657.

809 Gregg, M. C., T. B. Sanford, and D. P. Winkel (2003), Reduced mixing from the
810 breaking of internal waves in equatorial waters, *Nature*, *422*(6931), 513-515.

811 Guemas, V., D. Salas-Méla, M. Kageyama, H. Giordani, and A. Voltaire (2011),
812 Impact of the Ocean Mixed Layer Diurnal Variations on the Intraseasonal
813 Variability of Sea Surface Temperatures in the Atlantic Ocean, *J. Climate*, *24*,
814 2889-2914.

815 Guemas, V., D. Salas-Méla, M. Kageyama, H. Giordani, and A. Voltaire (2013),
816 Impact of the ocean diurnal cycle on the North Atlantic mean Sea Surface
817 Temperatures in a regionally coupled model, *Dyn. Atmos. Oceans*, *60*, 28-45.

818 Halliwell, G. R. (2004), Evaluation of vertical coordinate and vertical mixing
819 algorithms in the HYbrid-Coordinate Ocean Model (HYCOM), *Ocean Modell.*, *7*,
820 285-322.

821 Halpern, D., and R. K. Reed (1976), Heat budget of the upper ocean under light winds,

822 *J. Phys. Oceanogr.*, 6, 972-975.

823 Han, W., and J. P. McCreary (2001), Modeling salinity distributions in the Indian Ocean,
824 *J. Geophys. Res.*, 106, 859-877.

825 Han, W., T. Shinoda, L. L. Fu, and J. P. McCreary (2006), Impact of atmospheric
826 intraseasonal oscillations on the Indian Ocean Dipole during the 1990s, *J. Phys.*
827 *Oceanogr.*, 36, 670-690.

828 Han, W., D. Yuan, W. T. Liu, and D. Halkides (2007), Intraseasonal variability of
829 Indian Ocean sea surface temperature during boreal winter: Madden-Julian
830 Oscillation versus submonthly forcing and processes, *J. Geophys. Res.*, 112,
831 C04001, doi:10.1029/2006JC003791.

832 Han W., P. J. Webster, J. Lin, W. T. Liu and R. Fu, J. Lin and A. Hu (2008), Dynamics
833 of intraseasonal sea level and thermocline variability in the equatorial Atlantic
834 during 2002-2003, *J. Phys. Oceanogr.*, 38, 945-967.

835 Harrison, D. E., and G. A. Vecchi (2001), January 1999 Indian Ocean cooling event,
836 *Geophys. Res. Lett.*, 28, 3717–3720.

837 Hermes J. C, and C. J. C. Reason (2008), Annual cycle of the South Indian Ocean
838 (Seychelles–Chagos) thermocline ridge in a regional ocean model, *J. Geophys.*
839 *Res.*, 113, C04035, doi:10.1029/2007JC004363.

840 Hosoda, S., T. Ohira, and T. Nakamura (2008), A monthly mean dataset of global
841 oceanic temperature and salinity derived from Argo float observations, *JAMSTEC*
842 *Rep. Res. Dev.*, 8, 47-59.

843 Inness, P. M., and J. M. Slingo (2003), Simulation of the Madden-Julian oscillation in a
844 coupled general circulation model. Part I: Comparison with observations and an
845 atmosphere-only GCM, *J. Climate*, 16(3), 345-364.

846 Inness, P. M., J. M. Slingo, E. Guilyardi, and J. Cole (2003), Simulation of the
847 Madden-Julian Oscillation in a coupled general circulation model. Part II: The role
848 of the basic state, *J. Climate*, 16(3), 365-382.

849 Izumo, T., S. Masson, J. Vialard, C. de Boyer Montegut, S. K. Behera, G. Madec, K.
850 Takahashi, and T. Yamagata (2010), Low and high frequency Madden–Julian

851 oscillations in austral summer: interannual variations, *Clim. Dyn.*, *35*, 669-683.

852 Jayakumar, A., J. Vialard, M. Lengaigne, C. Gnanaseelan, J. P. McCreary, and B.
853 Praveen Kumar (2011), Processes controlling the surface temperature signature of
854 the Madden–Julian Oscillation in the thermocline ridge of the Indian Ocean, *Clim.*
855 *Dyn.*, *37*, 2217-2234.

856 Jayakumar, A., and C. Gnanaseelan (2012), Anomalous intraseasonal events in the
857 thermocline ridge region of Southern Tropical Indian Ocean and their regional
858 impacts, *J. Geophys. Res.*, *117*, C03021, doi:10.1029/2011JC007357.

859 Jerlov, N. G. (1976), *Marine Optics*, Elsevier Sci. Pub. Co. Amsterdam.

860 Jochum, M., and R. Murtugudde (2005), Internal variability of Indian ocean SST, *J.*
861 *Climate*, *18*(18), 3726-3738.

862 Kara, A. B., H. E. Hurlburt, and A. J. Wallcraft (2005), Stability-Dependent Exchange
863 Coefficients for Air-Sea Fluxes, *J. Atmos. Oceanic Tech.*, *22*, 1080-1094.

864 Kara, A., A. J. Wallcraft, P. J. Martin, and E. P. Chassignet (2008), Performance of
865 mixed layer models in simulating SST in the equatorial Pacific Ocean, *J. Geophys.*
866 *Res.*, *113*, C02020, doi:10.1029/2007JC004250.

867 Kawai, Y., and H. Kawamura (2002), Evaluation of the diurnal warming of sea surface
868 temperature using satellite-derived marine meteorological data, *J. Oceanogr.*, *58*,
869 805-814.

870 Kawai, Y., and A. Wada (2007), Diurnal sea surface temperature variation and its
871 impact on the atmosphere and ocean: a review, *J. Oceanogr.*, *63*, 721-744.

872 Kelly, K. A., L. Thompson, W. Cheng, and E. J. Metzger (2007), Evaluation of
873 HYCOM in the Kuroshio Extension region using new metrics, *J. Geophys. Res.*,
874 *112*, C01004, doi:10.1029/2006JC003614.

875 Kennedy, J., P. Brohan, and S. Tett (2007), A global climatology of the diurnal
876 variations in sea-surface temperature and implications for MSU temperature trends,
877 *Geophys. Res. Lett.*, *34*, L05712, doi:10.1029/2006GL028920.

878 Knutson, T. R., and K. M. Weickmann (1987), 30–60 day atmospheric oscillations:

879 composite life cycles of convection and circulation anomalies, *Mon. Wea. Rev.*,
880 115, 1407–1436.

881 Kummerow, C., W. Barnes, T. Kozu, J. Shiue, and J. Simpson (1998), The Tropical
882 Rainfall Measuring Mission (TRMM) sensor package, *J. Atmos. Oceanic Technol.*,
883 15, 809-817.

884 Large, W. G., G. Danabasoglu, S. C. Doney, and J. C. McWilliams (1997), Sensitivity
885 to surface forcing and boundary layer mixing in a global ocean model:
886 Annual-mean climatology, *J. Phys. Oceanogr.*, 27, 2418-2447.

887 Large, W. G., J. C. McWilliams, and S. C. Doney (1994), Ocean vertical mixing: A
888 review and a model with a nonlocal boundary layer parameterization, *Rev.*
889 *Geophys.*, 32, 363–403, doi:10.1029/94RG01872.

890 Lau, W. K., D. E. Waliser, K. Sperber, J. Slingo, and P. Inness (2012), Modeling
891 intraseasonal variability, in *Intraseasonal Variability in the Atmosphere-Ocean*
892 *Climate System*, 399-431, Springer Berlin Heidelberg.

893 Liebmann, B., and C. A. Smith (1996), Description of a complete (interpolated),
894 outgoing longwave radiation dataset, *Bull. Am. Meteorol. Soc.*, 77, 1275– 1277.

895 Lin, J. L., and coauthors (2006), Tropical intraseasonal variability in 14 IPCC AR4
896 climate models. part I: Convective signals, *J. Climate*, 19, 2665–2690.

897 Lloyd, I. D., and G. A. Vecchi (2010), Submonthly Indian Ocean cooling events and
898 their interaction with large-scale conditions, *J. Climate*, 23, 700-716.

899 Locarnini, R. A., A. V. Mishonov, J. I. Antonov, T. P. Boyer, H. E. Garcia, O. K.
900 Baranova, M. M. Zweng, and D. R. Johnson (2010), *World Ocean Atlas 2009*,
901 *Volume 1: Temperature*, S. Levitus, Ed. NOAA Atlas NESDIS 68, U.S.
902 Government Printing Office, Washington, D.C., 184 pp.

903 Loeb, N. G., K. J. Priestley, D. P. Kratz, E. B. Geier, R. N. Green, B. A. Wielicki, P. O.
904 R. Hinton, and S. K. Nolan (2001), Determination of unfiltered radiances from the
905 Clouds and the Earth's Radiant Energy System instrument, *J. Appl. Meteor.*, 40,
906 822-835.

907 Madden, R. A., and P. R. Julian (1971), Detection of a 40–50 day oscillation in the

908 zonal wind in the tropical Pacific, *J. Atmos. Sci.*, *28*, 702-708.

909 Masson, S., P. Terray, G. Madec, J.-J. Luo, T. Yamagata, and K. Takahashi (2012),
910 Impact of intra-daily SST variability on ENSO characteristics in a coupled model,
911 *Clim. Dyn.*, *39*, 681–707.

912 McCreary, J. P., K. E. Kohler, R. R. Hood, S. Smith, J. Kindle, A. S. Fischer, and R. A.
913 Weller (2001), Influences of diurnal and intraseasonal forcing on mixed-layer and
914 biological variability in the central Arabian Sea, *J. Geophys. Res.*, *106*, 7139-7156.

915 McCreary J. P., P. K. Kundu, and R. L. Molinari (1993), A numerical investigation of
916 dynamics, thermodynamics and mixed layer processes in the Indian Ocean, *Prog.*
917 *Oceanogr.*, *31*, 181–244.

918 McPhaden, M. J., and Coauthors (2009), RAMA: The Research Moored Array for
919 African–Asian–Australian Monsoon Analysis and Pre-diction, *Bull. Amer. Meteor.*
920 *Soc.*, *90*, 459–480.

921 Metzger, E., H. Hurlburt, X. Xu, J. F. Shriver, A. Gordon, J. Sprintall, R. Susanto, and
922 H. van Aken (2010), Simulated and observed circulation in the Indonesian Seas:
923 1/12° global HYCOM and the INSTANT observations, *Dyn. Atmos. Oceans*, *50*,
924 275-300.

925 Noh, Y., E. Lee, D.-H. Kim, S.-Y. Hong, M.-J. Kim, and M.-L. Ou (2011), Prediction of
926 the diurnal warming of sea surface temperature using an atmosphere-ocean mixed
927 layer coupled model, *J. Geophys. Res.*, *116*, C11023, doi:10.1029/2011JC006970.

928 Nyadjro, E. S., B. Subrahmanyam, V. S. N. Murty, and J. F. Shriver (2012), The role of
929 salinity on the dynamics of the Arabian Sea mini warm pool, *J. Geophys. Res.*, *117*,
930 C09002, doi:10.1029/2012JC007978.

931 Oh, J.-H., B.-M. Kim, K.-Y. Kim, H.-J. Song, and G.-H. Lim (2012), The impact of the
932 diurnal cycle on the MJO over the Maritime Continent: a modeling study
933 assimilating TRMM rain rate into global analysis, *Clim. Dyn.*, *40*, 893–911.

934 Papa, F., F. Durand, W. B. Rossow, A. Rahman, and S. K. Bala (2010), Satellite
935 altimeter-derived monthly discharge of the Ganga-Brahmaputra River and its
936 seasonal to interannual variations from 1993 to 2008, *J. Geophys. Res.*, *115*,

937 C12013, doi:10.1029/2009JC006075.

938 Pimentel, S., K. Haines, and N. Nichols (2008), Modeling the diurnal variability of sea
939 surface temperatures, *J. Geophys. Res.*, *113*, C11004, doi:10.1029/2007JC004607.

940 Price, J. F., R. A. Weller, and R. Pinkel (1986), Diurnal Cycling: Observations and
941 Models of the Upper Ocean Response to Diurnal Heating, Cooling, and Wind
942 Mixing, *J. Geophys. Res.*, *91*(C7), 8411-8427.

943 Saji, N., S. P. Xie, and C. Y. Tam (2006), Satellite observations of intense intraseasonal
944 cooling events in the tropical south Indian Ocean, *Geophys. Res. Lett.*, *33*, L14704,
945 doi:10.1029/2006GL026525.

946 Sato, N., C. Takahashi, A. Seiki, K. Yoneyama, R. Shirooka, and Y. Takayabu (2009),
947 An evaluation of the reproducibility of the Madden-Julian oscillation in the CMIP3
948 multi-models, *J. Meteorol. Soc. Jpn.*, *87*, 791-805.

949 Saunders, P. M. (1967), The temperature at the ocean-air inter-face, *J. Atmos. Sci.*, *24*,
950 269– 273.

951 Schiller, A., and J. Godfrey (2003), Indian Ocean intraseasonal variability in an ocean
952 general circulation model, *J. Climate*, *16*, 21-39.

953 Schott, F. A., S. P. Xie, and J. P. McCreary Jr (2009), Indian Ocean circulation and
954 climate variability, *Rev. Geophys.*, *47*, RG1002, doi:10.1029/2007RG000245.

955 Sengupta, D., B. N. Goswami, and R. Senan (2001), Coherent intraseasonal oscillations
956 of ocean and atmosphere during the Asian summer monsoon, *Geophys. Res. Lett.*,
957 *28*, 4127– 4130.

958 Shinoda, T. (2005), Impact of the diurnal cycle of solar radiation on intraseasonal SST
959 variability in the western equatorial Pacific, *J. Climate*, *18*, 2628-2636.

960 Shinoda, T., W. Han, E. J. Metzger, and H. E. Hurlburt (2012), Seasonal Variation of
961 the Indonesian Throughflow in Makassar Strait, *J. Phys. Oceanogr.*, *42*,
962 1099-1123.

963 Shinoda, T., and H. H. Hendon (1998), Mixed layer modeling of intraseasonal
964 variability in the tropical western Pacific and Indian Oceans, *J. Climate*, *11*,

965 2668-2685.

966 Shinoda, T., H. H. Hendon, and J. Glick (1998), Intraseasonal variability of surface
967 fluxes and sea surface temperature in the tropical western Pacific and Indian
968 Oceans, *J. Climate*, *11*, 1685-1702.

969 Shinoda, T., T. Jensen, M. Flatau, S. Chen (2013a), Surface wind and upper ocean
970 variability associated with the Madden-Julian Oscillation simulated by the Coupled
971 Ocean/Atmosphere Mesoscale Prediction System (COAMPS). *Mon. Wea. Rev.*,
972 *141*, 2290–2307.

973 Shinoda, T., T. Jensen, M. Flatau, W. Han, and C. Wang (2013b), Large-scale oceanic
974 variability associated with the Madden-Julian oscillation during the
975 CINDY/DYNAMO field campaign from satellite observations, *Remote Sensing*, *5*,
976 2072-2092.

977 Slingo, J., P. Inness, R. Neale, S. Woolnough, and G. Yang (2003), Scale interactions
978 on diurnal to seasonal timescales and their relevance to model systematic errors,
979 *Ann. Geophys.*, *46*, 139-155.

980 Smith, W. H. F., and D. T. Sandwell (1997), Global sea floor topography from satellite
981 altimetry and ship depth soundings, *Science*, *277*, 1956-1962.

982 Soloviev, A., and R. Lukas (1997), Observation of large diurnal warming events in the
983 near-surface layer of the western equatorial Pacific warm pool, *Deep-Sea Res.*,
984 *Part I*, *44*, 1055-1076.

985 Sperber, K. R., S. Gualdi, S. Legutke, and V. Gayler (2005), The Madden–Julian
986 oscillation in ECHAM4 coupled and uncoupled general circulation models, *Clim.*
987 *Dyn.*, *25*, 117-140.

988 Stommel, H., K. Saunders, W. Simmons, and J. Cooper (1969), Observations of the
989 diurnal thermocline, *Deep-Sea Res.*, *16*, 269-284.

990 Stramma, L., P. Cornillon, R. A. Weller, J. F. Price, and M. G. Briscoe (1986), Large
991 diurnal sea surface temperature variability: Satellite and in situ measurements, *J.*
992 *Phys. Oceanogr.*, *16*, 827-837.

993 Stuart-Menteth, A. C., I. S. Robinson, and P. G. Challenor (2003), A global study of

- 994 diurnal warming using satellite-derived sea surface temperature, *J. Geophys. Res.*,
995 108(C5), 3155, doi:10.1029/2002JC001534.
- 996 Sverdrup, H. U., R. H. Fleming, and M. W. Johnson (1942), *The oceans: their physics,*
997 *chemistry, and general biology*, Prentice-Hall New York
- 998 Terray, P., K. Kamala, S. Masson, G. Madec, A. Sahai, J.-J. Luo, and T. Yamagata
999 (2012), The role of the intra-daily SST variability in the Indian monsoon variability
1000 and monsoon-ENSO–IOD relationships in a global coupled model, *Clim. Dyn.*, 39,
1001 729–754.
- 1002 Thadathil, P., P. M. Muraleedharan, R. R. Rao, Y. K. Somayajulu, G. V. Reddy, and C.
1003 Revichandran (2007), Observed seasonal variability of barrier layer in the Bay of
1004 Bengal, *J. Geophys. Res.*, 112, C02009, doi:10.1029/2006JC003651.
- 1005 Vialard, J., J. Duvel, M. McPhaden, P. Bouruet-Aubertot, B. Ward, E. Key, D. Bourras,
1006 R. Weller, P. Minnett, and A. Weill (2009), Cirene: Air---Sea Interactions in the
1007 Seychelles---Chagos Thermocline Ridge Region, *Bull. Amer. Meteor. Soc.*, 90,
1008 45-61.
- 1009 Vialard, J., G. Foltz, M. J. McPhaden, J. P. Duvel, and C. de Boyer Montégut (2008),
1010 Strong Indian Ocean sea surface temperature signals associated with the
1011 Madden-Julian Oscillation in late 2007 and early 2008, *Geophys. Res. Lett.*, 35,
1012 L19608, doi:10.1029/2008GL035238.
- 1013 Vialard, J., A. Jayakumar, C. Gnanaseelan, M. Lengaigne, D. Sengupta, and B.
1014 Goswami (2011), Processes of 30–90 days sea surface temperature variability in
1015 the northern Indian Ocean during boreal summer, *Clim. Dyn.*, 38, 1901-1916.
- 1016 Vinayachandran, P. N., V. S. N. Murty, and V. Ramesh Babu (2002), Observations of
1017 barrier layer formation in the Bay of Bengal during summer monsoon, *J. Geophys.*
1018 *Res.*, 107(C12), 8018, doi:10.1029/2001JC000831.
- 1019 Vinayachandran, P., and N. Saji (2008), Mechanisms of south Indian Ocean
1020 intraseasonal cooling, *Geophys. Res. Lett.*, 35, L23607,
1021 doi:10.1029/2008GL035733.
- 1022 Waliser, D. E. (2005), Intraseasonal variability, *The Asian monsoon*, edited by B. Wang,

- 1023 Springer, Heidelberg, p844.
- 1024 Waliser, D. E., and N. E. Graham (1993), Convective cloud systems and warm-pool sea
1025 surface temperatures: Coupled interactions and self-regulation, *J. Geophys. Res.*,
1026 *98*(D7), 12881–12893.
- 1027 Waliser, D. E., K. Lau, and J. H. Kim (1999), The influence of coupled sea surface
1028 temperatures on the Madden-Julian oscillation: A model perturbation experiment, *J.*
1029 *Atmos. Sci.*, *56*, 333-358.
- 1030 Waliser, D. E., R. Murtugudde, and L. E. Lucas (2003), Indo-Pacific Ocean response to
1031 atmospheric intraseasonal variability: 1. Austral summer and the Madden-Julian
1032 Oscillation, *J. Geophys. Res.*, *108*, 3160, doi:10.1029/2002JC001620.
- 1033 Waliser, D. E., R. Murtugudde, and L. E. Lucas (2004), Indo-Pacific Ocean response to
1034 atmospheric intraseasonal variability: 2. Boreal summer and the Intraseasonal
1035 Oscillation, *J. Geophys. Res.*, *109*, C03030, doi:10.1029/2003JC002002.
- 1036 Wallcraft, A. J., E. J. Metzger, and S. N. Carroll (2009), Software design description for
1037 the HYbrid Coordinate Ocean Model (HYCOM) Version 2.2, Tech. Rep.
1038 NRL/MR/7320-09-9166 ,Nav.Res.Lab,Stennis Space Center, Miss.
- 1039 Wang, B., and H. Rui (1990), Synoptic climatology of transient tropical intraseasonal
1040 convection anomalies: 1975 – 1985, *Meteorol. Atmos. Phys.*, *44*, 43 – 61.
- 1041 Wang, B., and X. S. Xie (1998), Coupled modes of the warm pool climate system. Part
1042 1: The role of air-sea interaction in maintaining Madden-Julian Oscillation, *J.*
1043 *Climate*, *11*, 2116 – 2135.
- 1044 Wang, J.-W., W. Han, and R. L. Sriver (2012a), Impact of tropical cyclones on the
1045 ocean heat budget in the Bay of Bengal during 1999: 1. Model configuration and
1046 evaluation, *J. Geophys. Res.*, *117*, C09020, doi:10.1029/2012JC008372.
- 1047 Wang, J.-W., W. Han, and R. L. Sriver (2012b), Impact of tropical cyclones on the
1048 ocean heat budget in the Bay of Bengal during 1999: 2. Processes and
1049 interpretations, *J. Geophys. Res.*, *117*, C09021, doi:10.1029/2012JC008373.
- 1050 Watterson, I., and J. Syktus (2007), The influence of air–sea interaction on the
1051 Madden–Julian oscillation: The role of the seasonal mean state, *Clim. Dyn.*, *28*,

1052 703-722.

1053 Webber, B. G., A. J. Matthews, K. J. Heywood, and D. P. Stevens (2012), Ocean
1054 Rossby waves as a triggering mechanism for primary Madden–Julian events, *Q. J.
1055 R. Meteorol. Soc.*, *138*, 514–527.

1056 Webster, P. J., C. A. Clayson, and J. A. Curry (1996), Clouds, Radiation, and the
1057 Diurnal Cycle of Sea Surface Temperature in the Tropical Western Pacific, *J.
1058 Climate*, *9*, 1712-1730.

1059 Wentz, F. J., C. Gentemann, D. Smith, and D. Chelton (2000), Satellite measurements
1060 of sea surface temperature through clouds, *Science*, *288*, 847– 850.

1061 Wheeler M. C., and H. H. Hendon (2004), An all-season real-time multivariate MJO
1062 index: development of an index for monitoring and prediction, *Mon. Wea. Rev.*,
1063 *132*, 1917–1932.

1064 Wielicki, B. A., B. R. Barkstrom, E. F. Harrison, R. B. Lee III, G. Louis Smith, and J. E.
1065 Cooper (1996), Clouds and the Earth's Radiant Energy System (CERES): An earth
1066 observing system experiment, *Bull. Amer. Meteor. Soc.*, *77*, 853-868.

1067 Woolnough, S. J., J. M. Slingo, and B. J. Hoskins (2000), The relationship between
1068 convection and sea surface temperature on intraseasonal timescales, *J. Climate*, *13*,
1069 2086–2104.

1070 Woolnough, S. J., J. M. Slingo, and B. J. Hoskins (2001), The organization of tropical
1071 convection by intraseasonal sea surface temperature anomalies, *Q. J. R. Meteorol.
1072 Soc.*, *127*, 887-907.

1073 Woolnough, S. J., F. Vitart, and M. Balmaseda (2007), The role of the ocean in the
1074 Madden–Julian Oscillation: Implications for MJO prediction, *Q. J. R. Meteorol.
1075 Soc.*, *133*, 117-128.

1076 Xavier, P. K. (2012), Intraseasonal convective moistening in CMIP3 models, *J. Climate*,
1077 *25*, 2569 –2577.

1078 Xie, S.-P., H. Annamalai, F. A. Schott, and J. P. McCreary Jr (2002), Structure and
1079 mechanisms of south indian ocean climate variability, *J. Climate*, *15*, 864-878.

- 1080 Yang, J., Q. Bao, X. Wang, and T. Zhou (2012), The tropical intraseasonal oscillation in
1081 SAMIL coupled and uncoupled general circulation models, *Adv. Atmos. Sci.*, *29*,
1082 529-543.
- 1083 Yang, G.-Y., and J. Slingo (2001), The diurnal cycle in the tropics, *Mon. Wea. Rev.*, *129*,
1084 784-801.
- 1085 Yokoyama, R., S. Tanba, and T. Souma (1995), Sea surface effects on the sea surface
1086 temperature estimation by remote sensing, *Remote Sensing*, *16*, 227-238.
- 1087 Yoneyama, K., C. Zhang, and C. N. Long (2013), Tracking pulses of the Madden-Julian
1088 oscillation, *Bull. Amer. Meteorol. Soc.*, in press,
1089 doi:<http://dx.doi.org/10.1175/BAMS-D-12-00157.1>.
- 1090 Yuan, D., and W. Han (2006), Roles of equatorial waves and western boundary
1091 reflection in the seasonal circulation of the equatorial Indian Ocean, *J. Phys.*
1092 *Oceanogr.*, *36*, 930-944.
- 1093 Zhang, C. (2005), Madden-Julian oscillation, *Rev. Geophys.*, *43*, RG2003,
1094 doi:[10.1029/2004RG000158](https://doi.org/10.1029/2004RG000158).
- 1095 Zhang, C., and M. Dong (2004), Seasonality in the Madden-Julian oscillation, *J.*
1096 *Climate*, *17*, 3169-3180.
- 1097 Zhang, C., M. Dong, S. Gualdi, H. H. Hendon, E. D. Maloney, A. Marshall, K. R.
1098 Sperber, and W. Wang (2006), Simulations of the Madden-Julian oscillation in
1099 four pairs of coupled and uncoupled models, *Clim. Dyn.*, *27*, 573-592.
- 1100 Zhang, C., J. Gottschalck, E. D. Maloney, M. W. Moncrieff, F. Vitart, D. E. Waliser, B.
1101 Wang, and M. C. Wheeler (2013), Cracking the MJO nut, *Geophys. Res. Lett.*, *40*,
1102 1223-1230, doi:[10.1002/grl.50244](https://doi.org/10.1002/grl.50244).
- 1103 Zhang, X., Y. Lu, K. R. Thompson, J. Jiang, and H. Ritchie (2010), Tropical Pacific
1104 Ocean and the Madden-Julian Oscillation: Role of wind and buoyancy forcing, *J.*
1105 *Geophys. Res.*, *115*, C05022, doi:[10.1029/2009JC005734](https://doi.org/10.1029/2009JC005734).
- 1106 Zhao, C., T. Li, and T. Zhou (2013), Precursor signals and processes associated with
1107 MJO initiation over the tropical Indian Ocean, *J. Climate*, *26*, 291-307.

1108 Zhou, L., R. Murtugudde, and M. Jochum (2008), Dynamics of the intraseasonal
1109 oscillations in the Indian Ocean South Equatorial Current, *J. Phys. Oceanogr.*, 38,
1110 121-132.

1111 **Figure Captions**

1112 **Figure 1.** Comparison of daily surface net shortwave radiation Q_{SW} ($W m^{-2}$) between the
1113 CERES dataset (blue) and in-situ measurements of RAMA buoys (red) at (a) $80.5^{\circ}E, 0^{\circ}$,
1114 (b) $80.5^{\circ}E, 8^{\circ}S$, and (c) $90^{\circ}E, 1.5^{\circ}S$. A surface albedo of 3% was applied to the RAMA
1115 buoy data before plotting.

1116 **Figure 2.** Mean wintertime (November-April) SST ($^{\circ}C$) from (a) TMI satellite
1117 observation and (b) the HYCOM MR. Black vectors in (a) denotes the mean wintertime
1118 CCMP wind stress ($N m^{-2}$). Mean wintertime SSS (psu) from (c) the MOAA-GPV
1119 dataset and (d) the HYCOM MR. In all panels, variables are averaged for the period of
1120 January 2006 – November 2011. The two black rectangles denote the areas of the SCTR
1121 ($55^{\circ}-70^{\circ}E, 12^{\circ}-4^{\circ}S$) and CEIO ($65^{\circ}-95^{\circ}E, 3^{\circ}S-3^{\circ}N$) regions.

1122 **Figure 3.** Mean wintertime MLD (m) in the Indian Ocean basin during 2006-2011 from
1123 (a) the MOAA-GPV dataset and (b) HYCOM MR. Black contours' interval is 10 m. The
1124 two black rectangles denote the SCTR and CEIO.

1125 **Figure 4.** (a) SST time series ($^{\circ}C$) averaged over the Indian Ocean basin ($30^{\circ}-110^{\circ}E$,
1126 $36^{\circ}S-30^{\circ}N$) from TMI (red solid) and HYCOM MR (blue solid). The dashed straight
1127 lines denote their 2005-2011 mean values. (b) Mean temperature profiles for the SCTR
1128 region from the MOAA-GPV dataset (blue) and HYCOM MR (red). (c) is the same as
1129 (b) but for the CEIO region.

1130 **Figure 5.** Comparison of SST time series from RAMA buoys' in-situ measurements
1131 (green), TMI satellite observations (red), and HYCOM MR output (blue) at two sites
1132 representing (a) the SCTR region ($67^{\circ}E, 1.5^{\circ}S$) and (c) the CEIO region ($80.5^{\circ}E, 1.5^{\circ}S$).
1133 Right panels, (b) and (d), are their corresponding power spectrums (solid lines), with the
1134 dashed lines denoting 95% significance level. Here, power spectrums are calculated
1135 after a 20-90-day Lanczos band-pass filter to highlight the intraseasonal signals. SST of
1136 RAMA buoys are measured at 1.5-m depth.

1137 **Figure 6.** 1.5-m temperature ($^{\circ}C$) measured by a RAMA buoy (red) and HYCOM MR
1138 0.26-m temperature (blue) and 1.5-m temperature (green) at $95^{\circ}E, 5^{\circ}S$ during the
1139 CINDY/DYNAMO field campaign period covered by our model simulation. Data are
1140 presented in 0.1-day resolution.

1141 **Figure 7.** Depth-date maps of daily temperature ($^{\circ}\text{C}$) from DYNAMO buoys at (a) 79°E ,
1142 0° and (b) 78°E , 1.5°S , with the MLD highlighted with blue curves. (c) and (d) are the
1143 corresponding maps from HYCOM MR. (e) and (f) compare the daily SST anomaly ($^{\circ}\text{C}$)
1144 from DYNAMO buoys (red) and HYCOM MR (blue) at the two buoy sites.

1145 **Figure 8.** Mean fields of (a) SST difference (color shading; in $^{\circ}\text{C}$) and (b) MLD
1146 difference (color shading; in m) between MR and EXP, i.e., ΔSST and ΔMLD , in winter.
1147 Black contours denote mean winter SST and MLD from MR.

1148 **Figure 9.** STD maps of 20-90-day SST ($^{\circ}\text{C}$) from (a) TMI and (b) MR. (c) The
1149 difference of 20-90-day SST STD ($^{\circ}\text{C}$) between MR and EXP and (d) its ratio (%)
1150 relative to the EXP value. The two black rectangles denote the areas of the SCTR and
1151 CEIO. All the STD values are calculated for winter months (November-April) in
1152 2006-2011.

1153 **Figure 10.** 20-90-day OLR (W m^{-2}) averaged over (a) the SCTR region and (b) the
1154 CEIO region. The red straight lines indicate one STD value range. Wintertime OLR
1155 minima with magnitude exceeding 1.5 STD value are highlighted with red asterisks.
1156 Time series of 20-90-day SST ($^{\circ}\text{C}$) from MR (red) and EXP (blue) averaged over (c) the
1157 SCTR region and (d) the CEIO region.

1158 **Figure 11.** Evolutions of (a) 20-90-day OLR (pink; in W m^{-2}) and unfiltered τ_x (green;
1159 in N m^{-2}), (b) SST (in $^{\circ}\text{C}$), (c) MLD H (m), and (d) mean mixed layer heating Q/H (W
1160 m^{-3}) of the composite wintertime MJO event in the SCTR region. In (b)-(d), red (blue)
1161 curves denote variables of MR (EXP). (e)-(h) are the same as (a)-(d) but for the CEIO
1162 region.

1163 **Figure 12.** Mean fields of (a) surface diurnal warming $d\text{SST}$ ($^{\circ}\text{C}$), (b) shortwave
1164 radiation Q_{sw} (W m^{-2}), and (c) wind speed (color shading; in m s^{-1}) and wind stress
1165 (black vectors; in N m^{-2}) during the campaign period (9/16-11/29 2011). Here $d\text{SST}$ is
1166 defined as the difference between the MR SST maximum between 10:30 and 21:00 LST
1167 and the preceding minimum between 0:00 and 10:30 LST in each day. The two black
1168 rectangles denote the SCTR and CEIO.

1169 **Figure 13.** Upper panels: time-longitude plots of (a) 20-90-day OLR (W m^{-2}), (b)
1170 unfiltered zonal wind stress τ_x (N m^{-2}), (c) MR SSTA ($^{\circ}\text{C}$), and (d) ΔSST (in $^{\circ}\text{C}$)

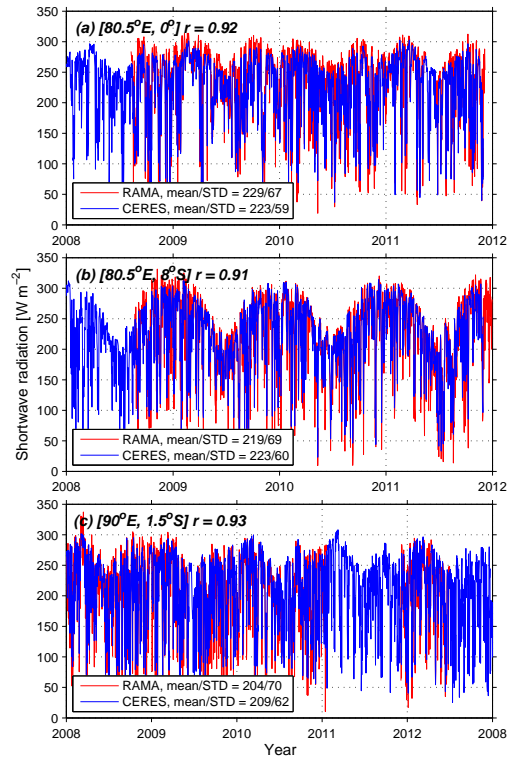
1171 averaged in the latitude range of the SCTR (12° - 4° S). The two dashed lines indicate the
1172 longitude range of the SCTR (55° - 70° E). Lower panels are the same as the uppers but in
1173 the latitude range of the CEIO (3° S- 3° N), with the two dashed lines indicating its
1174 longitude range (65° - 95° E). We defined six stages based on the 20-90-day OLR value in
1175 the CEIO region: 10/01-10/11, the calm stage of MJO 1 (CM-1); 10/11-10/21, the
1176 developing stage of the MJO 1 (DV-1); 10/21-10/29, the wet stage of the MJO 1 (WT-1);
1177 10/29-11/8, the decaying stage of MJO 1 (DC-1); 11/08-11/15, the calm stage of MJO 2
1178 (CM-2); and 11/15-11/29, the developing stage of MJO 2.

1179 **Figure 14.** Evolutions of (a) 20-90-day OLR (pink; in W m^{-2}) and unfiltered τ_x (green;
1180 in N m^{-2}), (b) SST ($^{\circ}\text{C}$), (c) MLD H (m), (d) mean mixed layer heating Q/H (W m^{-3}), (e)
1181 the MR-EXP difference in daily upward turbulent heat flux ΔQ_T (W m^{-2}), and (f) the Q_T
1182 diurnal cycle (W m^{-2}) averaged in the SCTR region. In (b)-(d), grey, red, and blue
1183 curves denote respectively the variables from 0.1-day MR output, daily MR output, and
1184 daily EXP output. (g)-(l) are the same as (a)-(f) but for the CEIO region.

1185 **Figure 15.** (a) Root-mean-squared (rms) SST difference ($^{\circ}\text{C}$) between MR and EXP,
1186 ΔSST , and (b) STD of 120-day high-passed SSH (cm) from MR in winter. (c) Time
1187 series of 20-90-day SST at the site 85°E , 15°S from MR (red) and EXP (blue). (d) is the
1188 same as (c) but for the 20-90-day SST averaged over the region 80° - 90°E , 20° - 10°S .
1189 The black asterisk and rectangle in (a) and (b) denote respectively the site for (c) and
1190 region for (d).

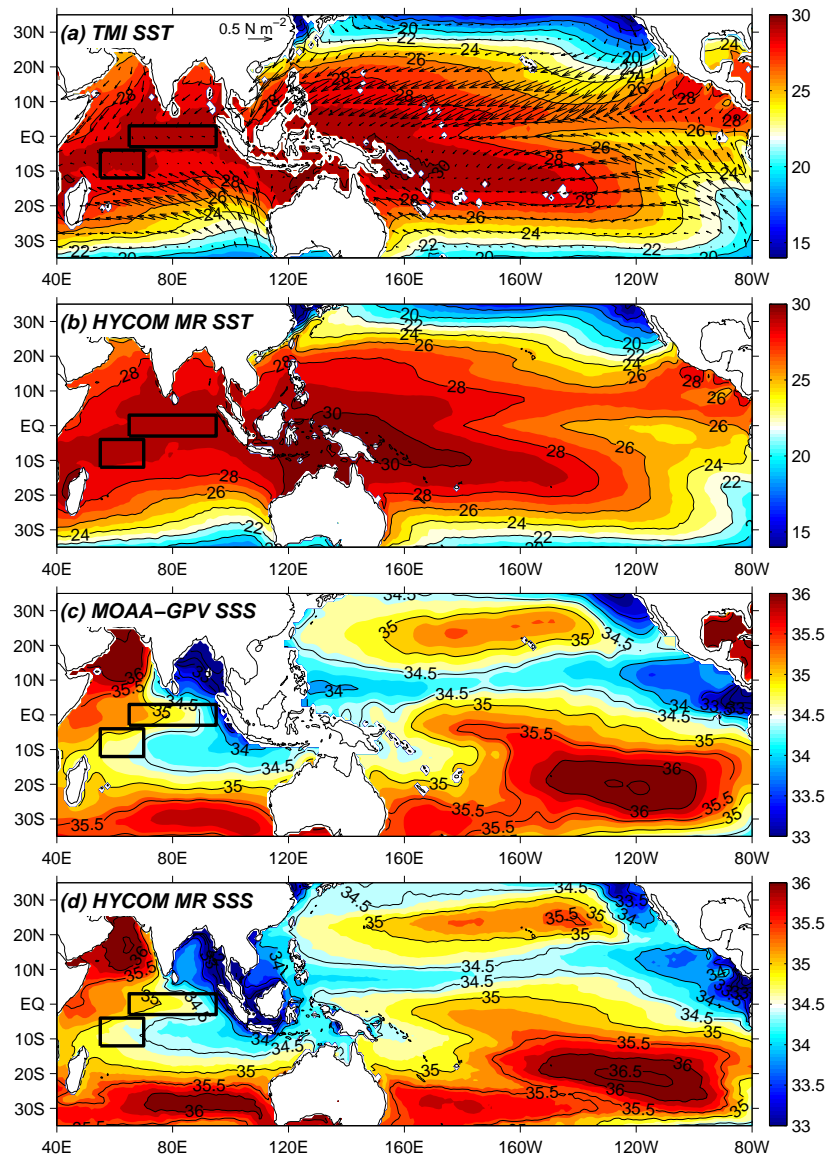
1191 **Figure 16.** Time-longitude plots of daily SSHA (cm) from (a) MR and (b) EXP, and (c)
1192 their difference ΔSSHA averaged in the latitude range of the SCTR (12° - 4° S).

1 Figures



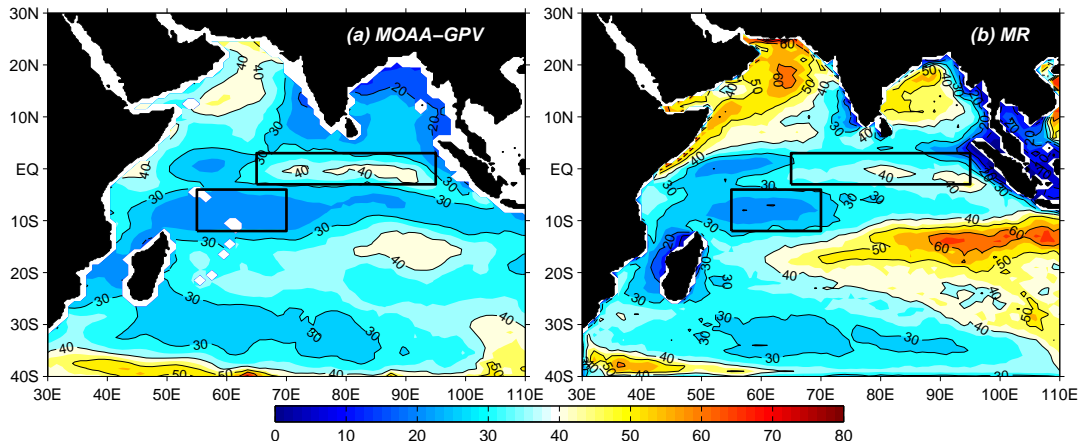
2

3 **Figure 1.** Comparison of daily surface net shortwave radiation Q_{SW} ($W m^{-2}$) between the
4 CERES dataset (blue) and in-situ measurements of RAMA buoys (red) at (a) $80.5^{\circ}E, 0^{\circ}$,
5 (b) $80.5^{\circ}E, 8^{\circ}S$, and (c) $90^{\circ}E, 1.5^{\circ}S$. A surface albedo of 3% was applied to the RAMA
6 buoy data before plotting.



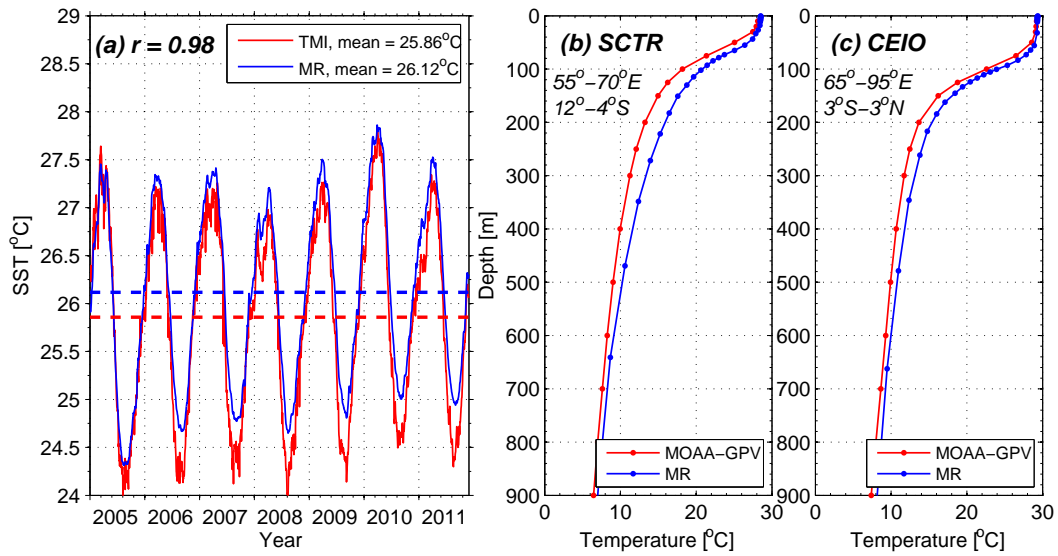
7

8 **Figure 2.** Mean wintertime (November-April) SST (°C) from (a) TMI satellite
 9 observation and (b) the HYCOM MR. Black vectors in (a) denotes the mean wintertime
 10 CCMP wind stress ($N m^{-2}$). Mean wintertime SSS (psu) from (c) the MOAA-GPV
 11 dataset and (d) the HYCOM MR. In all panels, variables are averaged for the period of
 12 January 2006 – November 2011. The two black rectangles denote the areas of the SCTR
 13 (55°-70°E, 12°-4°S) and CEIO (65°-95°E, 3°S-3°N) regions.



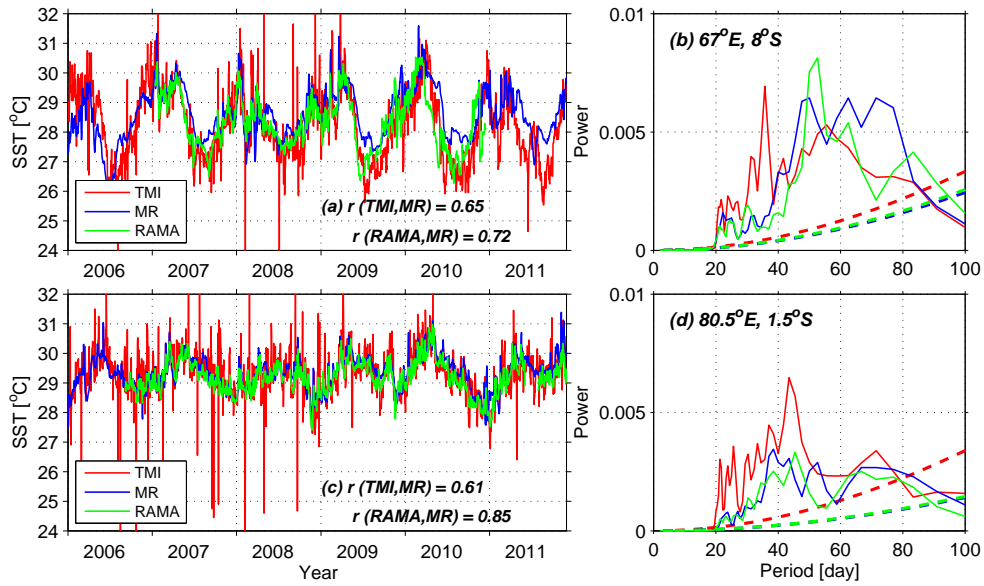
14

15 **Figure 3.** Mean wintertime MLD (m) in the Indian Ocean basin during 2006-2011 from
 16 (a) the MOAA-GPV dataset and (b) HYCOM MR. Black contours' interval is 10 m. The
 17 two black rectangles denote the SCTR and CEIO.



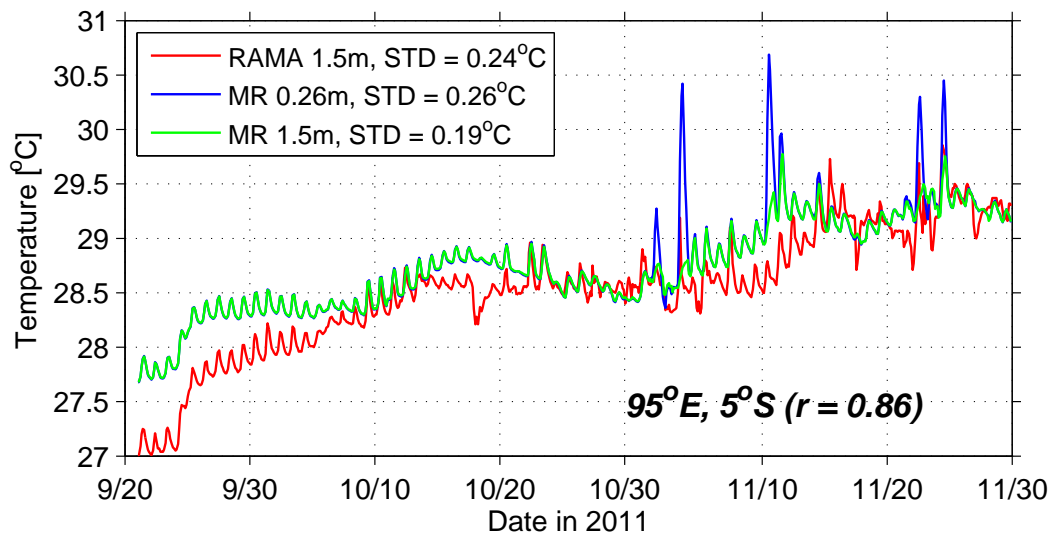
18

19 **Figure 4.** (a) SST time series (°C) averaged over the Indian Ocean basin (30°-110°E,
 20 36°S-30°N) from TMI (red solid) and HYCOM MR (blue solid). The dashed straight
 21 lines denote their 2005-2011 mean values. (b) Mean temperature profiles for the SCTR
 22 region from the MOAA-GPV dataset (blue) and HYCOM MR (red). (c) is the same as
 23 (b) but for the CEIO region.



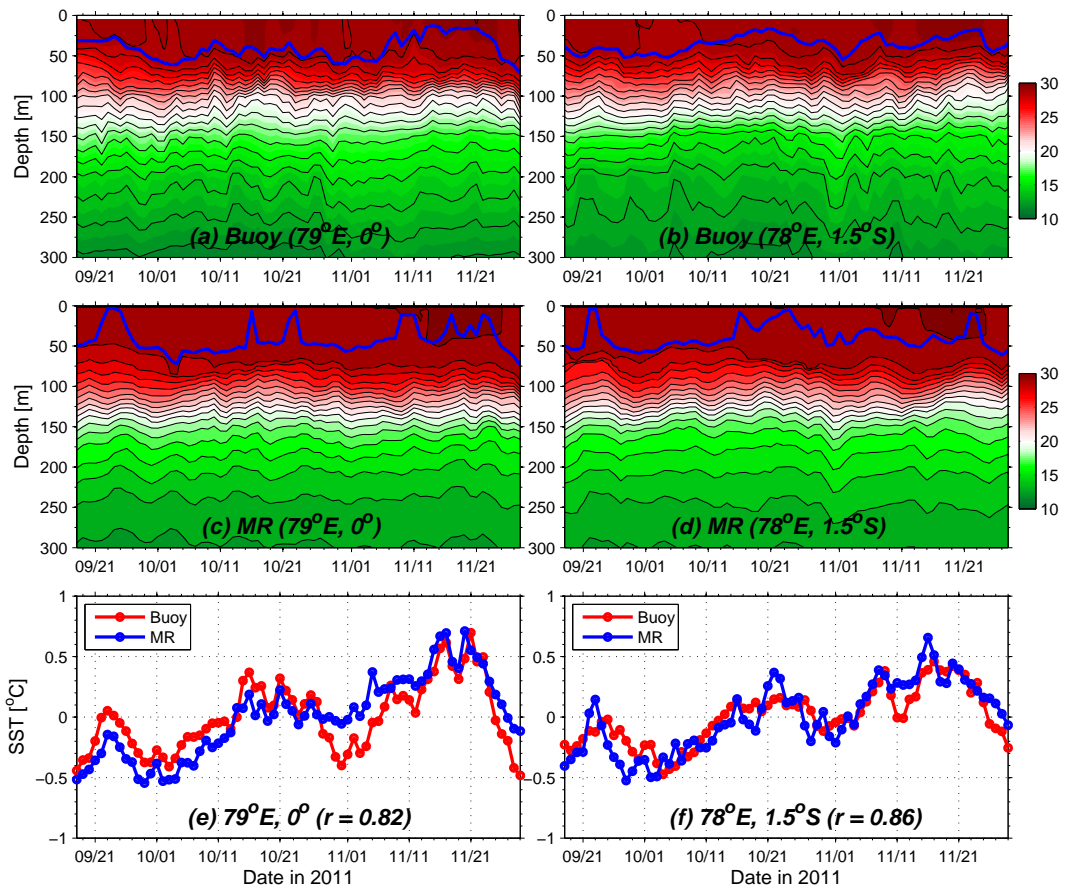
24

25 **Figure 5.** Comparison of SST time series from RAMA buoys' in-situ measurements
 26 (green), TMI satellite observations (red), and HYCOM MR output (blue) at two sites
 27 representing (a) the SCTR region (67°E, 1.5°S) and (c) the CEIO region (80.5°E, 1.5°S).
 28 Right panels, (b) and (d), are their corresponding power spectrums (solid lines), with the
 29 dashed lines denoting 95% significance level. Here, power spectrums are calculated
 30 after a 20-90-day Lanczos band-pass filter to highlight the intraseasonal signals. SST of
 31 RAMA buoys are measured at 1.5-m depth.



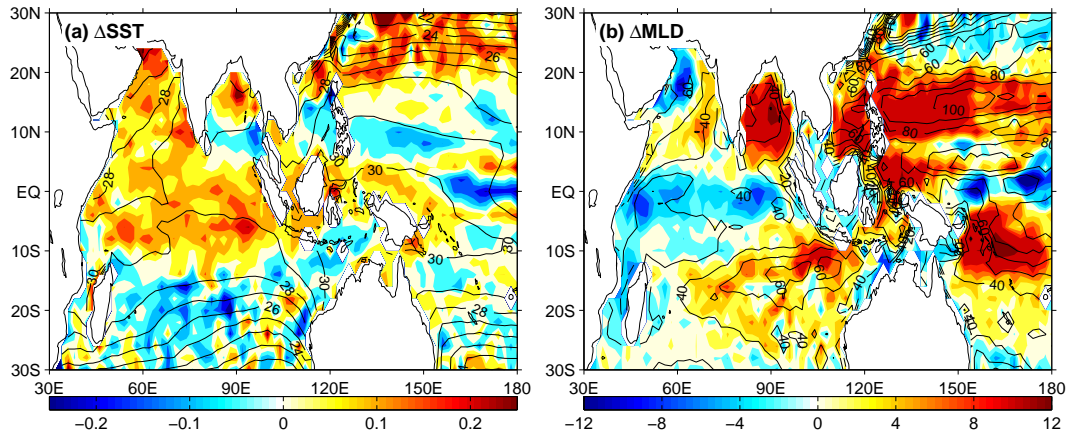
32

33 **Figure 6.** 1.5-m temperature (°C) measured by a RAMA buoy (red) and HYCOM MR
 34 0.26-m temperature (blue) and 1.5-m temperature (green) at 95°E, 5°S during the
 35 CINDY/DYNAMO field campaign period covered by our model simulation. Data are
 36 presented in 0.1-day resolution.



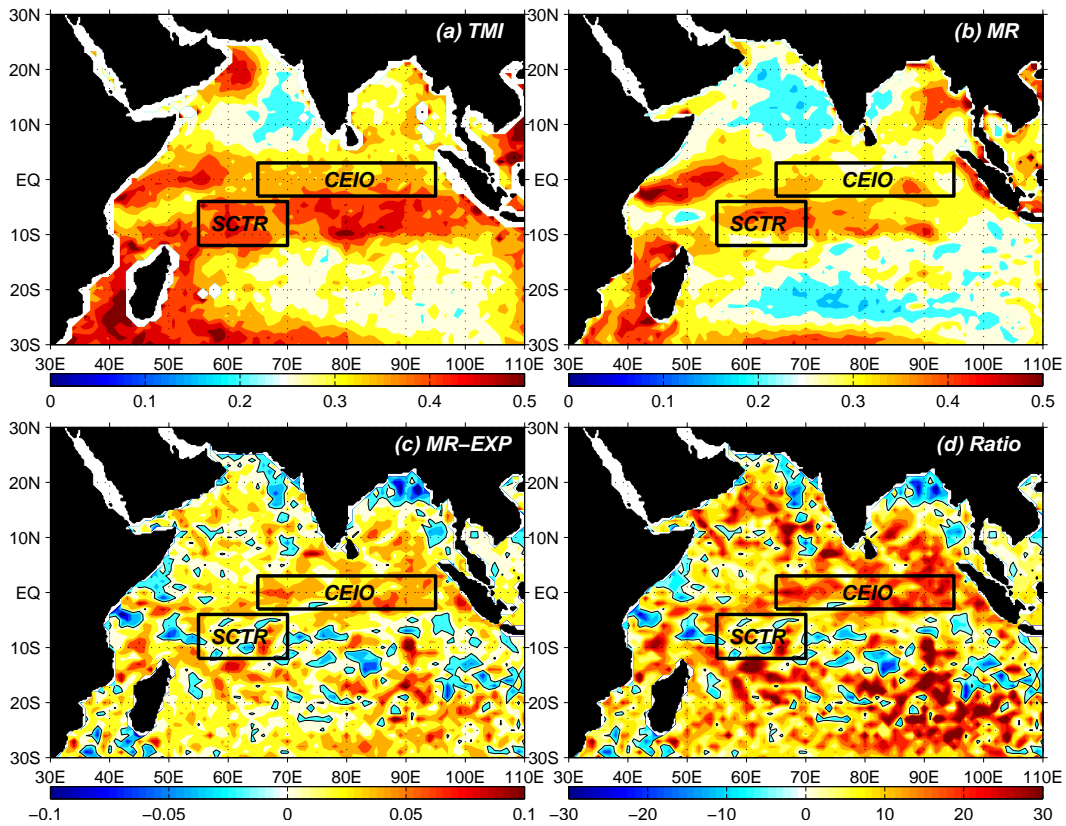
37

38 **Figure 7.** Depth-date maps of daily temperature ($^{\circ}\text{C}$) from DYNAMO buoys at (a) 79°E ,
 39 0° and (b) 78°E , 1.5°S , with the MLD highlighted with blue curves. (c) and (d) are the
 40 corresponding maps from HYCOM MR. (e) and (f) compare the daily SST anomaly ($^{\circ}\text{C}$)
 41 from DYNAMO buoys (red) and HYCOM MR (blue) at the two buoy sites.



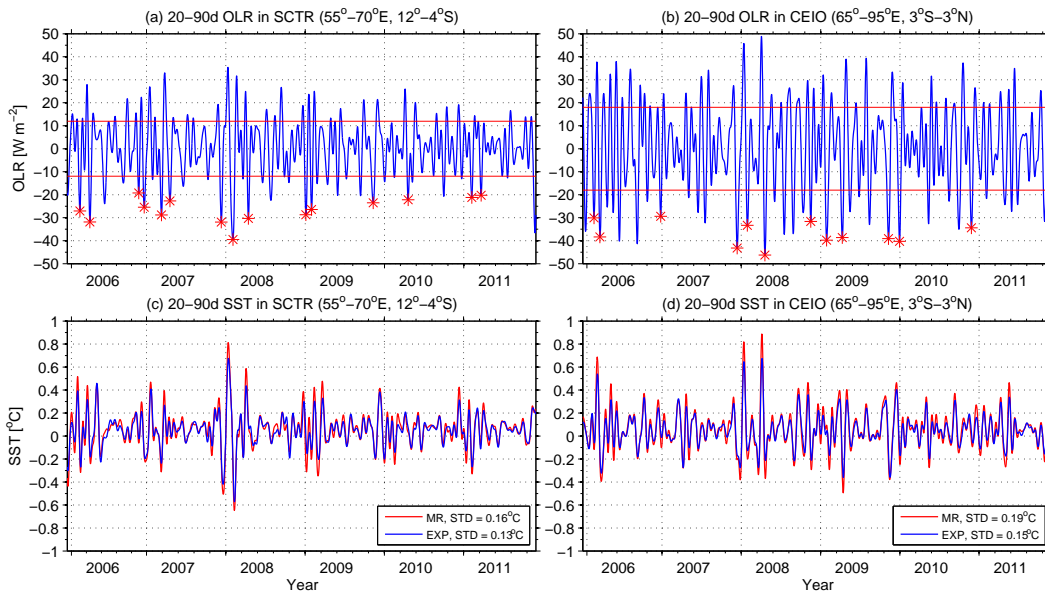
42

43 **Figure 8.** Mean fields of (a) SST difference (color shading; in °C) and (b) MLD
 44 difference (color shading; in m) between MR and EXP, i.e., Δ SST and Δ MLD, in winter.
 45 Black contours denote mean winter SST and MLD from MR.



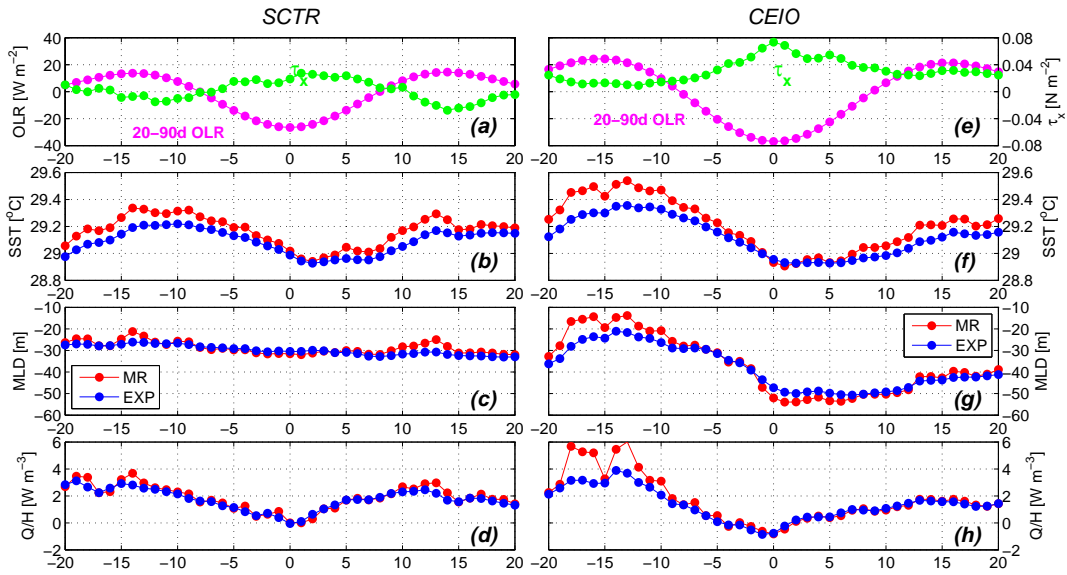
46

47 **Figure 9.** STD maps of 20-90-day SST (°C) from (a) TMI and (b) MR. (c) The
 48 difference of 20-90-day SST STD (°C) between MR and EXP and (d) its ratio (%)
 49 relative to the EXP value. The two black rectangles denote the areas of the SCTR and
 50 CEIO. All the STD values are calculated for winter months (November-April) in
 51 2006-2011.



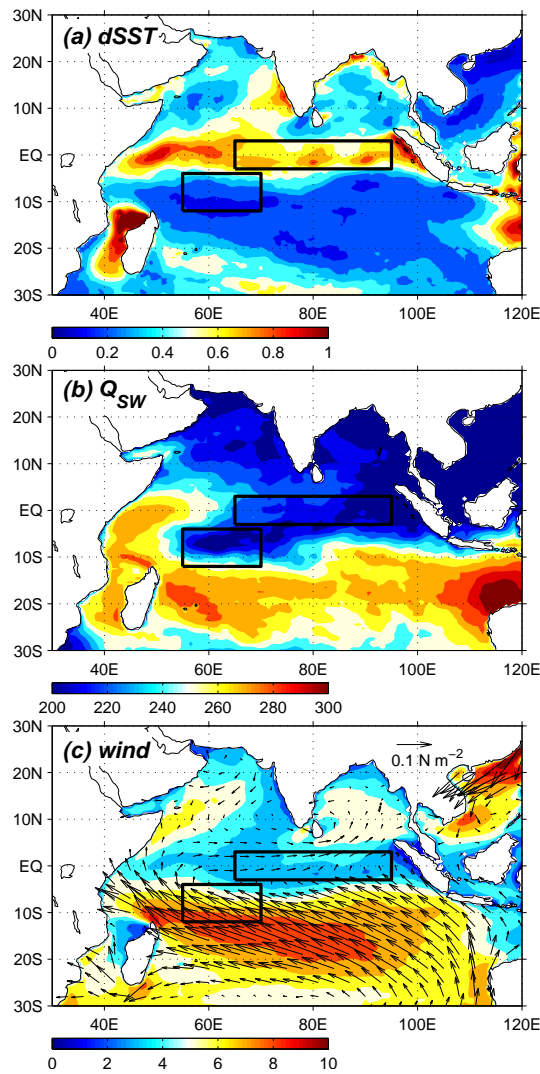
52

53 **Figure 10.** 20-90-day OLR (W m^{-2}) averaged over (a) the SCTR region and (b) the
 54 CEIO region. The red straight lines indicate one STD value range. Wintertime OLR
 55 minima with magnitude exceeding 1.5 STD value are highlighted with red asterisks.
 56 Time series of 20-90-day SST ($^{\circ}\text{C}$) from MR (red) and EXP (blue) averaged over (c) the
 57 SCTR region and (d) the CEIO region.



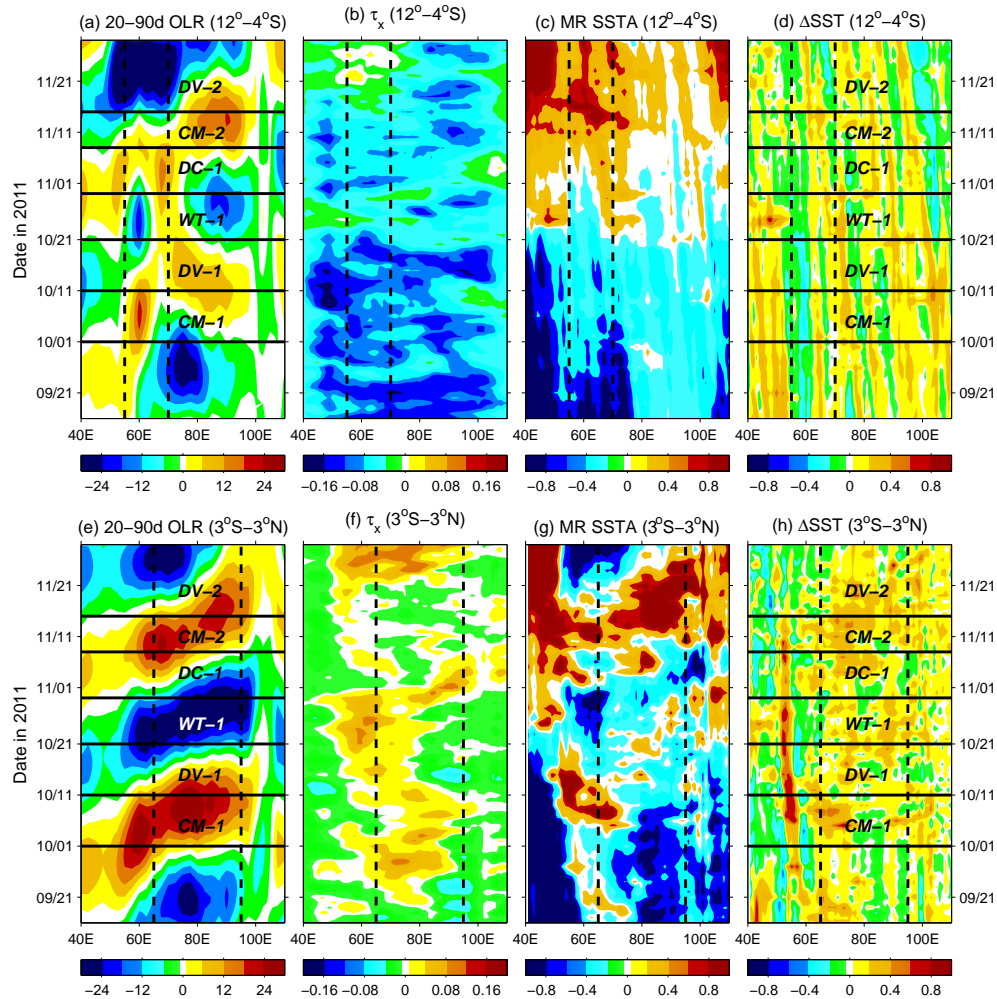
58

59 **Figure 11.** Evolutions of (a) 20-90-day OLR (pink; in W m^{-2}) and unfiltered τ_x (green;
 60 in N m^{-2}), (b) SST (in $^{\circ}\text{C}$), (c) MLD H (m), and (d) mean mixed layer heating Q/H (W
 61 m^{-3}) of the composite wintertime MJO event in the SCTR region. In (b)-(d), red (blue)
 62 curves denote variables of MR (EXP). (e)-(h) are the same as (a)-(d) but for the CEIO
 63 region.



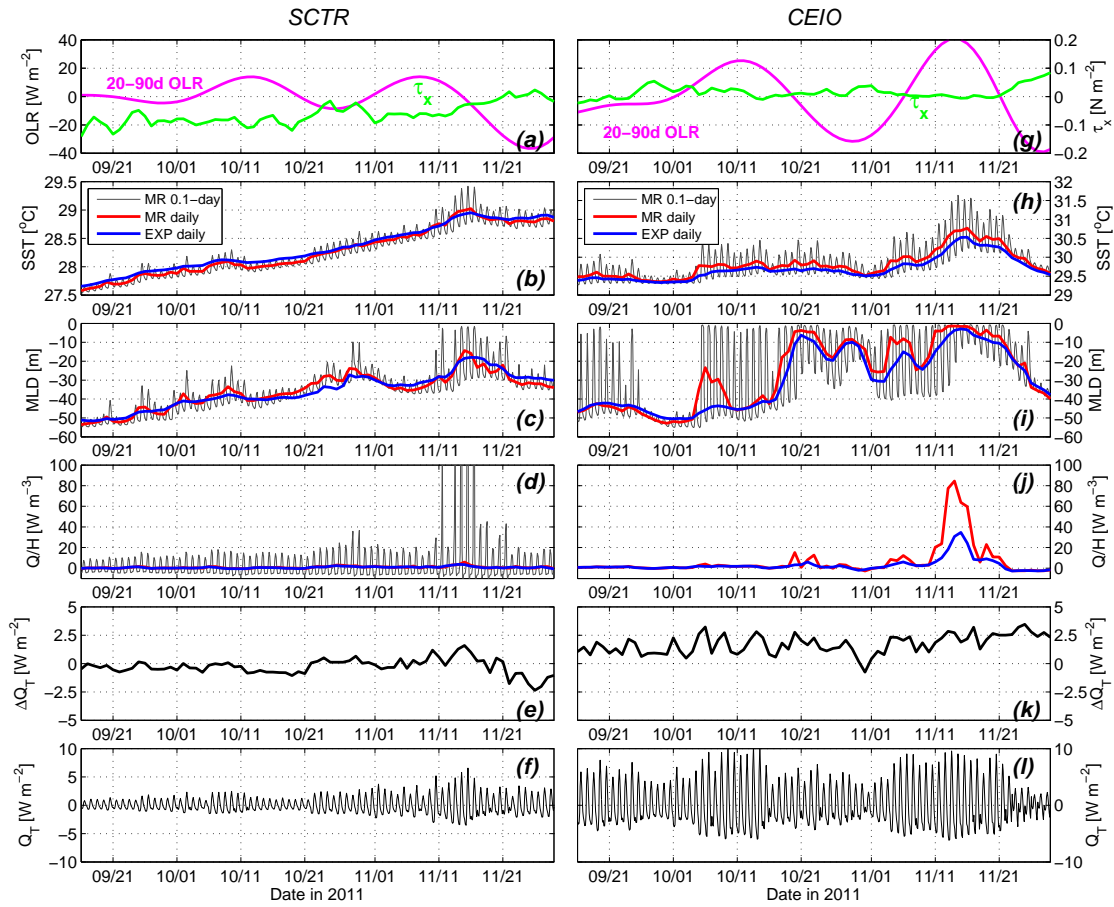
64

65 **Figure 12.** Mean fields of (a) surface diurnal warming $dSST$ ($^{\circ}C$), (b) shortwave
 66 radiation Q_{SW} ($W m^{-2}$), and (c) wind speed (color shading; in $m s^{-1}$) and wind stress
 67 (black vectors; in $N m^{-2}$) during the campaign period (9/16-11/29 2011). Here $dSST$ is
 68 defined as the difference between the MR SST maximum between 10:30 and 21:00 LST
 69 and the preceding minimum between 0:00 and 10:30 LST in each day. The two black
 70 rectangles denote the SCTR and CEIO.



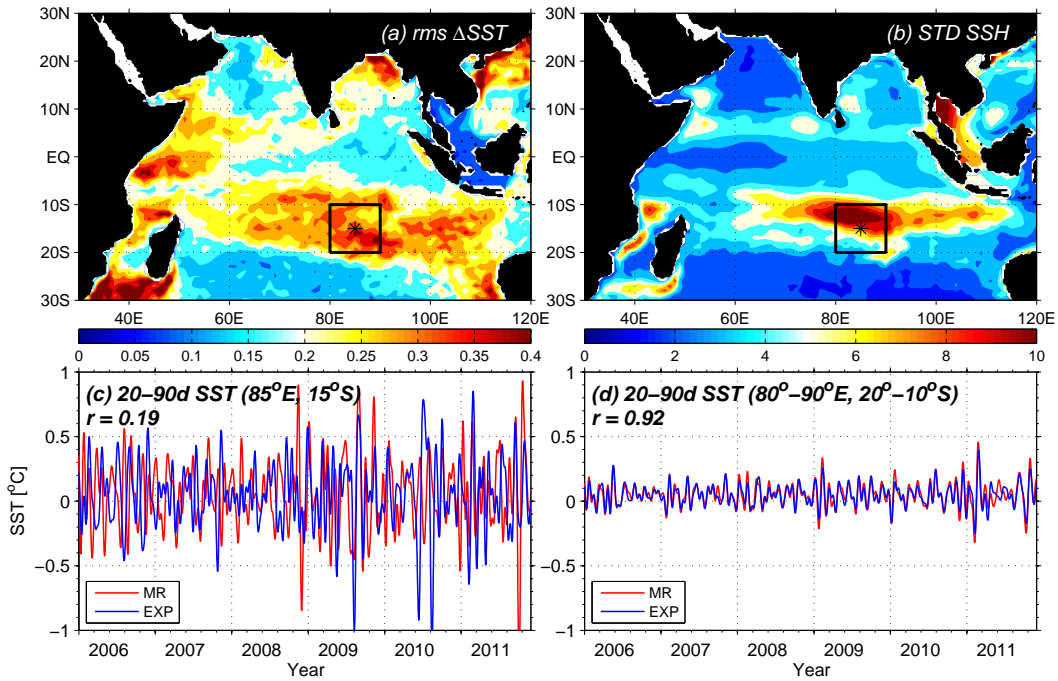
71

72 **Figure 13.** Upper panels: time-longitude plots of (a) 20-90-day OLR (W m^{-2}), (b)
 73 unfiltered zonal wind stress τ_x (N m^{-2}), (c) MR SSTA ($^{\circ}\text{C}$), and (d) ΔSST (in $^{\circ}\text{C}$)
 74 averaged in the latitude range of the SCTR ($12^{\circ}\text{-}4^{\circ}\text{S}$). The two dashed lines indicate the
 75 longitude range of the SCTR ($55^{\circ}\text{-}70^{\circ}\text{E}$). Lower panels are the same as the uppers but in
 76 the latitude range of the CEIO ($3^{\circ}\text{S}\text{-}3^{\circ}\text{N}$), with the two dashed lines indicating its
 77 longitude range ($65^{\circ}\text{-}95^{\circ}\text{E}$). We defined six stages based on the 20-90-day OLR value in
 78 the CEIO region: 10/01-10/11, the calm stage of MJO 1 (CM-1); 10/11-10/21, the
 79 developing stage of the MJO 1 (DV-1); 10/21-10/29, the wet stage of the MJO 1 (WT-1);
 80 10/29-11/8, the decaying stage of MJO 1 (DC-1); 11/08-11/15, the calm stage of MJO 2
 81 (CM-2); and 11/15-11/29, the developing stage of MJO 2.



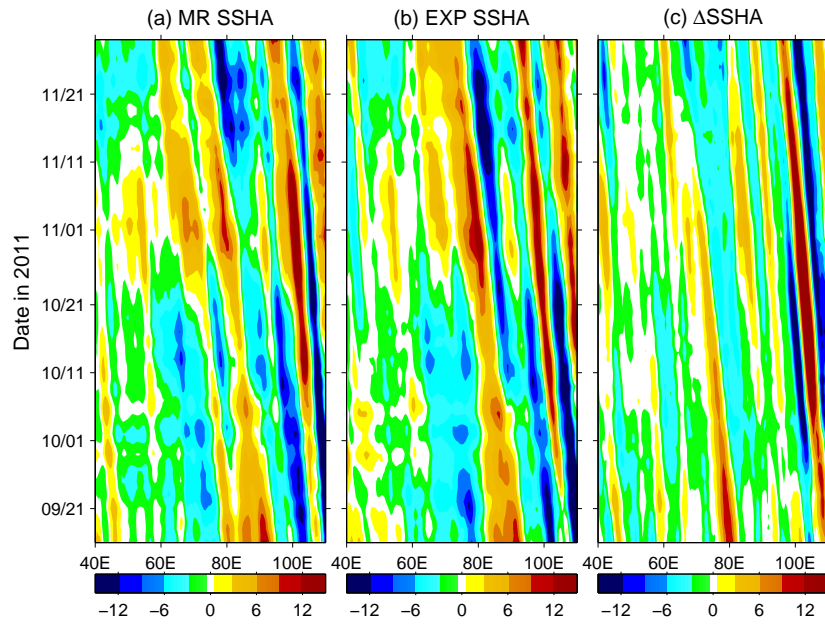
82

83 **Figure 14.** Evolutions of (a) 20-90-day OLR (pink; in W m^{-2}) and unfiltered τ_x (green;
 84 in N m^{-2}), (b) SST ($^{\circ}\text{C}$), (c) MLD H (m), (d) mean mixed layer heating Q/H (W m^{-3}), (e)
 85 the MR-EXP difference in daily upward turbulent heat flux ΔQ_T (W m^{-2}), and (f) the Q_T
 86 diurnal cycle (W m^{-2}) averaged in the SCTR region. In (b)-(d), grey, red, and blue
 87 curves denote respectively the variables from 0.1-day MR output, daily MR output, and
 88 daily EXP output. (g)-(l) are the same as (a)-(f) but for the CEIO region.



89

90 **Figure 15.** (a) Root-mean-squared (rms) SST difference (°C) between MR and EXP,
 91 Δ SST, and (b) STD of 120-day high-passed SSH (cm) from MR in winter. (c) Time
 92 series of 20-90-day SST at the site 85°E, 15°S from MR (red) and EXP (blue). (d) is the
 93 same as (c) but for the 20-90-day SST averaged over the region 80°-90°E, 20°-10°S.
 94 The black asterisk and rectangle in (a) and (b) denote respectively the site for (c) and
 95 region for (d).



96

97 **Figure 16.** Time-longitude plots of SSHA (cm) from (a) MR and (b) EXP, and (c) their
 98 difference Δ SSHA averaged for the latitudes of the SCTR (12° - 4° S).